

# Studies of a sample of 6C radio galaxies at redshift one, I – Deep multi–frequency radio observations

P. N. Best,<sup>1</sup> S. A. Eales,<sup>2</sup> M. S. Longair,<sup>3</sup> S. Rawlings<sup>4</sup> and H. J. A. Röttgering<sup>1</sup>

<sup>1</sup> *Sterrewacht Leiden, Postbus 9513, 2300 RA Leiden, The Netherlands*

<sup>2</sup> *Department of Physics and Astrophysics, University of Wales Cardiff, P.O.Box 913, Cardiff, CF2 3YB, United Kingdom*

<sup>3</sup> *Cavendish Astrophysics, Madingley Road, Cambridge, CB3 0HE, United Kingdom*

<sup>4</sup> *Department of Astrophysics, University of Oxford, Keble Road, Oxford, OX1 3RH, United Kingdom*

24 September 2018

## ABSTRACT

Deep radio observations at 5 and 8 GHz are presented of a complete sample of 11 radio galaxies with redshifts  $0.85 < z < 1.5$ , selected from the 6C sample of Eales. The radio data, taken using the Very Large Array in A, B and C array configurations, provide a best angular resolution of 0.25 arcseconds and reach an rms noise level of order  $20\mu\text{Jy}$ . Radio spectral index, radio polarisation, and rotation measure maps are also presented for each source, and the radio data are compared to K–band infrared images of the fields of these sources.

Radio core candidates are detected in eight of the eleven sources. Nine of the eleven sources display deviations from ‘standard double radio source’ morphologies, with multiple hotspots in one or both lobes, or a hotspot withdrawn from the leading edge of the radio emission. At 8 GHz, the sources are typically polarised at the 5 to 15% level. The mean rotation measures of the individual lobes are, in all but one case, less than  $50\text{ rad m}^{-2}$ , but strong asymmetries between the two lobes and steep gradients within some lobes indicate that the Faraday rotation does not have a Milky Way origin; rather, the distant 6C radio sources lie in a relatively dense clumpy environment.

The sources are compared with the more radio powerful 3CR radio galaxies in the same redshift range, and with low redshift radio galaxies. The ratio of core to extended radio flux is found to be almost independent of the linear size of a radio source and only weakly inversely correlated with the total radio source power. This latter result indicates that the high radio luminosity of the most powerful radio sources must originate in a powerful active nucleus, in contrast to the suggestion of some authors that such sources are so luminous only because confinement by a dense surrounding environment boosts the lobe fluxes. Environmental effects must play a secondary role.

**Key words:** Galaxies: active — Radio continuum: galaxies — Infrared: galaxies — Galaxies: jets — Polarisation

## 1 INTRODUCTION

The revised 3CR radio source catalogue, defined by Laing, Riley and Longair (1983), consists of the most powerful radio galaxies in the northern sky, selected at 178 MHz. The revised 3CR sample has long been fully identified optically, and is now also 100% spectroscopically complete. Until recently, no other low–frequency selected radio source sample even approached spectroscopic completeness.

The distant ( $z \sim 1$ ) 3CR radio sources have been the targets of numerous studies at a wide range of wavelengths (see e.g. McCarthy 1993 for a review). Of particular importance have been questions as to the nature of the host galaxies of these radio sources, the age of their stellar pop-

ulations, the environment in which the galaxies live, and the origin of their extremely powerful radio emission. These studies have led to a number of surprising results, not least of which were the very tight relationship between the infrared K–magnitudes and the redshifts of these galaxies (e.g. Lilly and Longair 1984), and the discovery that the optical and ultraviolet emission of these galaxies is elongated and aligned along the direction of the radio axis (Chambers et al. 1987; McCarthy et al. 1987). Discerning the dependence of these properties upon the radio power of the radio source is critical for determining the true nature of these objects.

We are involved in a long–running programme to understand the astrophysics of a sample of 28 3CR radio galaxies at redshift  $z \sim 1$ , using observations in the optical wave-

bands with the Hubble Space Telescope (HST), at radio wavelengths with the Very Large Array (VLA), and in the near-infrared using the United Kingdom InfraRed Telescope (UKIRT) (Longair et al. 1995; Best et al. 1996; Best et al. 1997; Best et al. 1998b). In order to understand how these 3CR radio galaxies relate to the less powerful radio galaxies, we have begun a project to study a matched sample of eleven galaxies selected from the 6C/B2 sample of radio galaxies (Eales 1985) over a similar redshift range. At any given redshift, these radio sources are about a factor of six lower in radio luminosity than those selected from the 3CR catalogue. Spectroscopic redshifts are currently available for 98% of the 6C/B2 sample (Rawlings et al. 1998), making this an ideal sample for comparison with the 3CR radio galaxies.

In this paper we present deep radio observations at 8 and 5 GHz of these galaxies. In Section 2, we discuss the selection of the current sample, the radio and infrared observations, and the data reduction. The results of the current work are presented in Section 3, in the form of maps and images of the radio emission of the sources, and its polarisation properties, at the various frequencies. The properties of the radio sources are also tabulated. Infrared K-band images of the fields of all but one of the radio galaxies, published by Eales et al (1997), are compared with the radio maps. In Section 4 we compare the 6C sources to other radio galaxy samples, and our results are summarised in Section 5. Presentation of the Hubble Space Telescope images of the 6C galaxies and a discussion of the differences between the optical/ultraviolet properties of the two samples is deferred to a later paper (Best et al. in preparation, hereafter Paper II).

## 2 OBSERVATIONS AND DATA REDUCTION

### 2.1 The sample

The current sample of radio galaxies was drawn from the complete sample of 59 radio sources from the 6CER sample (Rawlings et al. 1998), a revised version of the sample originally defined by Eales (1985). These radio sources have flux densities at 151 MHz which fall in the range  $2.0 \text{ Jy} < S_{151} < 3.93 \text{ Jy}$ , and lie in the region of the sky  $08^{\text{h}}20^{\text{m}} < \text{RA} < 13^{\text{h}}01^{\text{m}}$ ,  $34^{\circ} < \text{Dec} < 40^{\circ}$ . Our sample was restricted to those sources identified as radio galaxies and with redshifts in the range  $0.85 < z < 1.5$ . 1212+38, whose redshift has recently been revised downwards and now falls within our redshift range, is not included in our subsample because at the time the project was begun its redshift fell outside our selection criteria. 1123+34 was excluded from the subsample due to its small angular extent ( $\approx 0.5$  arcsec), which would make it barely resolvable in the 5 GHz observations. This leaves a sample of 11 radio galaxies.

### 2.2 Very Large Array observations

Observations of all eleven radio galaxies were made at 8 GHz and 5 GHz using the A-array configuration of the VLA on December 8th, 9th and 10th, 1996. For ten of the sources a 50 MHz bandwidth was used at each frequency, but for the largest source, 1011+36, a 25 MHz bandwidth was used

**Table 1.** Details of the VLA observations

Source	$z$	Frequencies [MHz]	Array config.	Observing Date	Int. time [min]
0825+34	1.46	4535,4885	A	10/12/96	39
		8085,8335	A	09/12/96	103
0943+39	1.04	4535,4885	A	10/12/96	39
		8085,8335	A	08/12/96	105
1011+36	1.04	4535,4885	B	24/02/97	60
			A	10/12/96	38
			C	17/09/97	12
		8085,8335	A	08/12/96	170
			B	24/02/97	61
			C	17/09/97	33
1017+37	1.05	4535,4885	A	10/12/96	39
		8085,8335	A	09/12/96	91
			A	10/12/96	39
1019+39	0.92	4535,4885	A	10/12/96	39
		8085,8335	A	10/12/96	100
1100+35	1.44	4535,4885	A	10/12/96	39
			B	24/02/97	21
			A	08/12/96	70
		8085,8335	A	09/12/96	33
			B	24/02/97	61
			A	10/12/96	39
1129+37	1.06	4535,4885	A	10/12/96	39
			B	24/02/97	21
			A	09/12/96	105
		8085,8335	B	24/02/97	61
			A	10/12/96	38
			A	09/12/96	104
1204+35	1.37	4535,4885	B	24/02/97	60
			A	10/12/96	39
			A	08/12/96	105
1217+36	1.09	4535,4885	A	10/12/96	39
		8085,8335	A	10/12/96	105
1256+36	1.07	4535,4885	A	10/12/96	39
			B	24/02/97	21
			A	08/12/96	105
		8085,8335	B	24/02/97	62
			A	10/12/96	39
			B	24/02/97	22
1257+36	1.00	4535,4885	C	17/09/97	11
			A	09/12/96	105
			B	24/02/97	62
		8085,8335	C	17/09/97	33

for the 8 GHz observations to avoid chromatic aberration effects. The largest angular scales that can be imaged using the A-array of the VLA at 5 and 8 GHz are about 11 and 8 arcsec respectively. Sources larger than these sizes were also imaged using the B-array configuration; these observations were made on February 24th, 1997. Similarly, the two largest sources were imaged using the C-array configuration on September 17th 1997. Details of the observations are given in Table 1.

The observations were carried out using standard VLA procedures. Short observations of the primary flux calibrator 3C286 were used to calibrate the flux density scale, and observations of this source separated in time by 6 hours determined the absolute polarisation position angle. The uncertainty in the calibration of the position angles, estimated from the difference between the solutions for the scans of 3C286, was about  $\pm 2$  degrees at each frequency. For observations at 4710 and 8210 MHz this corresponds to an uncertainty in the absolute value of the rotation measure of

about  $20 \text{ rad m}^{-2}$ . Secondary calibrators within a few degrees of each source were observed approximately every 25 minutes to provide accurate phase calibration; observations of these calibrators were spaced over a wide range of parallactic angles enabling the on-axis antenna polarisation response terms to be determined.

The data were reduced using the AIPS software provided by the National Radio Astronomy Observatory, with the two IFs at each frequency being reduced separately. The data from each different array configuration were individually CLEANed using the AIPS task IMAGR, and then one or two cycles of phase self-calibration were used to improve further the map quality. The  $uv$  data from the lower resolution array configurations were self-calibrating with those of the highest resolution array, a combined dataset was then produced, and a further cycle of phase self-calibration was carried out.

### 2.3 The radio maps

For each source, images were made at full angular resolution in the Stokes parameters I, Q and U, at both 8 and 5 GHz by CLEANing the final datasets using the AIPS task IMAGR. The full-width-half-maxima (FWHM) of the Gaussian restoring beams used for each map are provided in the figure captions. The Stokes I images of the two IFs at each frequency were combined to produce single total intensity maps at 8210 and at 4710 MHz.

Spectral index, rotation measure, depolarisation measure and magnetic field position angle maps of the sources were made following the method outlined by Best et al. (1998a). In brief, images of the 8 GHz data were made at the resolution of the 5 GHz data by applying an upper cut-off in the  $uv$  data matching the longest baseline sampled at 5 GHz, together with  $uv$  tapering to maintain the smooth coverage of the  $uv$  plane. Using these matched resolution datasets, maps of the spectral index,  $\alpha$ , (where  $I_\nu \propto \nu^{-\alpha}$ ) were made in regions of the images with surface brightnesses in excess of 5 times the rms noise level at both frequencies. Rotation measures were derived from the polarisation position angles at the four frequencies 4535, 4885, 8085 and 8335 MHz, in regions where the polarised intensity was detected in excess of four times the noise level at all frequencies. The depolarisation measure,  $DM_{8.2}^{4.7}$ , defined as the ratio of the fractional polarisation at 4710 MHz to that at 8210 MHz, was determined on a pixel by pixel basis, after correcting for Ricean bias in the total polarised intensity images, for pixels in which the total polarised intensity at both frequencies exceeding five times the noise level.

### 2.4 The infrared data

Infrared K-band images of all of these galaxies except 1019+39 have been taken during three observing runs, using the IRCAM and IRCAM3 cameras on the United Kingdom Infrared Telescope (UKIRT) and the REDEYE camera on the Canada–France–Hawaii Telescope (CFHT). These data were presented and described by Eales et al. (1997). Here, we present a comparison of this K-band data with the new radio data.

Uncertainties in the relative alignment of the infrared and radio reference frames may result in astrometric errors between the radio and infrared images of about an arcsecond: the errors are largest when no fiducial stars are present within the small field of view of the infrared cameras. For the eight galaxies for which a core candidate was detected  $\lesssim 1$  arcsec from the infrared galaxy, the relative alignment of the two frames was improved by assuming the radio core to be co-incident with the centroid of the infrared emission. Such alignment was possible to an accuracy of about 0.2 arcsec. For the two galaxies in which no radio core was identified, the infrared and radio images were simply overlaid assuming the two reference frames to be accurately registered.

## 3 RESULTS

In Figures 1 to 11, maps of the radio data are provided for each source. Shown in each figure are the 8 GHz radio map made at the highest angular resolution, the 5 GHz radio map, the polarisation position angle of the electric field vectors at 8 GHz, the magnetic field direction determined wherever a rotation measure could be derived, greyscale plots of the spectral index, the rotation measure and the depolarisation measure, calculated as described in the previous section, and finally (except for 1019+39) the infrared K-band image of the field of each radio source. Important parameters of each source are provided in Table 2, and are determined for the various components of the source in Table 3.

Some words of caution should be added here concerning the interpretation of the greyscale figures for spectral index, depolarisation and rotation measures, and of the fractional polarisations given in Tables 2 and 3. The inability of the CLEAN procedure to accurately represent smooth extended low-surface brightness emission can lead to artefacts in the spectral index maps, with such regions appearing speckled. This is particularly noticeable for 1011+36, 1257+36, and the western lobe of 1100+35 (Figures 3e, 6e and 11e), but can be seen at fainter levels in other sources. The globally averaged spectral indices of these regions, presented in Table 3, consider all of the low surface brightness emission regardless of how CLEAN has distributed it, and so are reliable. In addition, polarised flux in regions of low surface brightness may be removed by the Ricean bias correction, leading to these regions lacking polarisation and rotation measure data; this means that the fractional polarisations quoted in Tables 2 and 3 for sources containing such regions could better be considered as lower limits, especially for the largest sources. The depolarisation measures, however, are limited to regions where polarised emission is measured at both frequencies, and so do give accurate values. The global properties shown in the rotation measure greyscales can be demonstrated to be fully reliable using fits of the polarisation position angle against a  $\lambda$ -squared law; however, individual large variations seen in areas of only 2–3 pixels, particularly towards the extremities, should be treated with caution.

### 3.1 Notes on individual radio sources

A brief description of the structures of the individual radio sources is provided below.

**Table 2.** Properties of the radio sources. Total fluxes are measured from the lowest resolution data at each frequency, to ensure that all of the large-scale structure is sampled. They are quoted to the nearest mJy, as determined from these maps; these values are subject to errors of up to a few per cent due to the limited accuracy of the absolute calibration of the VLA. The fractional polarisation at each frequency was derived by dividing the flux density of the total polarised intensity map, after correction for Ricean bias, by that of the total intensity map, and is therefore a scalar rather than vector average of the polarisation. As discussed in the text, the Ricean bias correction may also lead to null polarisation measurements from low surface brightness regions which are polarised, particularly for the largest sources; therefore the fractional polarisations quoted should strictly be treated as lower limits, and no estimate of the error in this measurement is made. The largest angular size of a source is as measured between the centres of the compact emission region in each lobe which is most distant from the AGN; this measurement has an associated error  $\lesssim 0.1''$ . The separation quotient,  $Q$ , is defined as the ratio of the angular separations of the hotspots in the longer and shorter arms from the nucleus (tabulated in Table 3). The core fraction is calculated as the ratio of the flux density of the compact central component to that of the extended radio emission at 8 GHz. Where a core candidate is not detected, an upper limit for the core fraction is derived assuming the core flux density to be below five times the rms noise level. The beam sizes of the radio maps are provided in the individual figure captions.

Source	RA (J2000) Dec		Total Flux	Frac. Polaris.	RMS Noise	Total Flux	Frac. Polaris.	RMS Noise	Largest Angular Size	$Q$	Core Fraction
			8210 MHz			4710 MHz					8210 MHz
			[mJy]	[%]	[ $\mu$ Jy]	[mJy]	[%]	[ $\mu$ Jy]	[ $''$ ]		
0825+34	08 28 26.85	34 42 49.1	45	6.9	18	87	6.3	22	7.0	$1.53 \pm 0.07$	$0.0053 \pm 0.0004$
0943+39	09 46 18.71	39 44 18.5	45	7.7	15	78	2.7	26	10.6	$3.44 \pm 0.05$	$0.0049 \pm 0.0003$
1011+36	10 14 12.90	36 17 18.0	52	2.7	19	87	2.9	26	51.0	$1.26 \pm 0.01$	$0.0943 \pm 0.0005$
1017+37	10 20 40.03	36 57 02.3	57	8.0	19	109	6.7	23	7.4	$3.48 \pm 0.21$	$0.0021 \pm 0.0003$
1019+39	10 22 55.25	39 08 49.9 <sup>a</sup>	73	10.6	20	139	7.2	24	7.9	$1.3 \pm 0.4$	$<0.0014$
1100+35	11 03 26.26	34 49 47.2	56	8.0	14	99	7.5	28	13.1	$1.40 \pm 0.03$	$0.124 \pm 0.001$
1129+37	11 32 35.35	36 54 17.8 <sup>a</sup>	75	16.8	14	134	15.3	22	16.1	$1.7 \pm 0.3$	$<0.0009$
1204+35	12 07 31.86	35 03 06.2	62	11.8	14	117	9.1	27	17.4	$1.55 \pm 0.03$	$0.021 \pm 0.0002$
1217+36	12 20 09.83	36 29 07.1	111	5.5	23	163	4.6	45	4.3	—	$\lesssim 0.67^b$
1256+36	12 59 06.07	36 31 58.2 <sup>a</sup>	97	10.6	15	172	10.3	25	17.5	$1.25 \pm 0.20$	$<0.0008$
1257+36	12 59 30.02	36 17 03.0 <sup>c</sup>	40	7.8	12	73	7.1	26	38.9	$1.14 \pm 0.01$	$0.0032 \pm 0.0003^c$

<sup>a</sup> Positions taken from optical IDs.

<sup>b</sup> Core fraction probably overestimated: see text.

<sup>c</sup> Assuming that the core is the NW candidate. If it is the SE candidate then the position is RA: 12 59 30.13, Dec: +36 17 02.0, and the core fraction is  $0.0055 \pm 0.0003$ .

*0825 + 34* : This source shows a strong asymmetry in flux between its two lobes, but the new detection of an inverted spectrum radio core roughly co-incident with the optical identification of Eales et al. (1997) at redshift  $z = 1.46$  (Rawlings et al. 1998), demonstrates that this source is an asymmetric double rather than a core-jet source (c.f. Naundorf et al. 1992). The south-eastern arm contains double hotspots. The polarisation properties are strongly asymmetric, with the north-western lobe having little depolarisation at 5 GHz whilst the south-eastern emission is completely depolarised.

*0943 + 39* : A flat-spectrum radio core is detected for the first time, co-incident with the proposed identification of a galaxy with redshift  $z = 1.04$  (Eales et al. 1997). The eastern lobe shows very strong depolarisation and, on the 8 GHz image, the radio emission appears to bend sharply at the location of the current hotspot. The western arm is also depolarised, although much less so, and has a uniform, relatively flat spectral index.

*1011 + 36* : The largest source in the current sample, 1011+36 has a bright, inverted-spectrum radio core, and is associated with a galaxy with redshift  $z = 1.04$  (Eales et al. 1997), rather than the original identification close to the northern radio lobe proposed by Allington-Smith et al. (1982; see also Naundorf et al. 1992, Law-Green et al. 1995). This original identification is not even detected on our K-band image (Figure 3h). The image does, however, show two

faint companions within five arcsecs of the host galaxy, and aligned close to the radio axis.

The south-western lobe of the source contains a second, compact hotspot. In the 1.4 GHz image of Law-Green et al. the lobe emission of the northern arm extends back to the core, but its surface brightness at 5 GHz is too low for this to be apparent on our map. The source shows low polarisation, but practically no depolarisation between 5 and 8 GHz. It is possible that owing to the low surface brightness of many of the features of this radio source, a significant fraction of the true polarised intensity will have been lost during the Ricean bias removal.

*1017 + 37* : First identified by Lilly (1989), the radio galaxy which hosts 1017+37 ( $z = 1.05$ , Rawlings et al. 1998, also known as 4C37.27A) lies close to the north-eastern lobe, and for the first time a faint core candidate is detected co-incident with this. The source shows a large asymmetry both in the angular sizes of its lobes, and in their rotation measures; the rotation measures of the lobes differ by nearly  $150 \text{ rad m}^{-2}$  in the rest-frame of the source.

*1019 + 39* : Also known as 4C39.31, this radio source was identified with a galaxy at redshift  $z = 0.921$  by Allington-Smith et al. (1985; see also Thompson et al. 1994). No radio core is detected in the current observations. The south-western lobe is the more compact, and contains a second bright hotspot. The two radio lobes are reasonably symmetric in their depolarisations and spectral indices, but differ by about  $200 \text{ rad m}^{-2}$  in their rest-frame rotation measures.

**Table 3.** Properties of the various components of the radio sources. Total fluxes and fractional polarisations are as defined in Table 2. Unless explicitly stated, errors in the total flux measurements are of order a few per cent due to calibration uncertainties. Fractional polarisations, as discussed for Table 2, are strictly lower limits. The spectral indices are the mean values for that region of the source, calculated between 4710 and 8210 MHz; assuming 3% uncertainties in the absolute calibration at each frequency gives a systematic uncertainty in the absolute spectral indices of 0.07. Uncertainties due to measurement errors of individual features are quoted when comparable to or larger than this systematic error. The depolarisation measures quoted are the mean values of the pixel by pixel ratios of the scalar fractional polarisation at 4710 and 8210 MHz in each region; in this way, they are unaffected by regions in which polarisation is too low to be measured. The errors represent the error on the mean in these regions. The rotation measures and their errors are the mean values from the frequencies 4535, 4885, 8085 and 8335 MHz determined in a similar way. The angular size quoted for each lobe is the angular separation between the radio core and the most distant compact emission region in the lobe. Where a radio core is detected these are measured to an accuracy  $\lesssim 0.1''$ ; in the three cases where the optical ID is used, the accuracy is only  $\sim 1$  arcsec.

Source	Component	Total Flux 8210 MHz [mJy]	Fractional Polarization 8210 MHz [%]	Total Flux 4710 MHz [mJy]	Fractional Polarization 4710 MHz [%]	Spectral Index $\alpha$	Depolar. Measure $DM_{8.2}^{4.7}$	Rotation Measure $RM$ [rad m $^{-2}$ ]	Angular Size [ $''$ ]
0825+34	Core	$0.24 \pm 0.018$	0.0	$0.16 \pm 0.022$	0.0	$-0.73 \pm 0.28$	—	—	—
	SE lobe	2.6	1.9	4.6	0.0	1.04	0.0	—	4.2
	NW lobe	42.4	7.1	82.1	6.6	1.19	$0.94 \pm 0.04$	$14 \pm 2$	2.75
0943+39	Core	$0.22 \pm 0.015$	0.0	$0.20 \pm 0.026$	0.0	$-0.18 \pm 0.26$	—	—	—
	E lobe	21.9	9.2	44.3	1.4	1.27	$0.22 \pm 0.01$	$26 \pm 2$	2.4
	W lobe	22.6	6.5	33.8	4.4	0.73	$0.84 \pm 0.02$	$12 \pm 2$	8.25
1011+36	Core	4.9	0.0	4.0	0.0	-0.33	—	—	—
	N lobe	32.9	3.1	56.9	3.1	0.99	$1.02 \pm 0.02$	$41 \pm 2$	22.8
	S lobe	13.9	2.7	26.2	2.9	1.15	$0.91 \pm 0.02$	$15 \pm 1$	28.8
1017+37	Core	$0.12 \pm 0.019$	0.0	$0.10 \pm 0.023$	0.0	$-0.24 \pm 0.50$	—	—	—
	NE lobe	34.4	6.9	66.7	5.8	1.19	$0.78 \pm 0.07$	$-13 \pm 5$	1.65
	SW lobe	22.4	9.6	40.1	8.3	1.04	$0.87 \pm 0.02$	$22 \pm 3$	5.75
1019+39	NE lobe	28.7	11.6	54.2	8.5	1.14	$0.88 \pm 0.01$	$38 \pm 3$	4.5 <sup>a</sup>
	SW lobe	45.1	9.6	84.9	6.4	1.14	$0.81 \pm 0.04$	$89 \pm 4$	3.5 <sup>a</sup>
1100+35	Core	6.9	0.0	6.8	0.0	-0.04	—	—	—
	'Jet'	7.0	6.8	11.1	4.3	0.82	$0.86 \pm 0.02$	$23 \pm 2$	—
	E lobe	12.7	9.7	21.7	9.6	0.96	$1.01 \pm 0.02$	$10 \pm 3$	7.7
	W lobe	29.1	9.5	57.0	8.5	1.21	$0.91 \pm 0.01$	$17 \pm 1$	5.5
1129+37	NW lobe	30.0	9.6	52.8	8.3	1.02	$0.91 \pm 0.02$	$-13 \pm 2$	6 <sup>a</sup>
	SE lobe	45.5	21.3	80.9	19.9	1.03	$0.93 \pm 0.01$	$3 \pm 2$	10 <sup>a</sup>
1204+35	Core	$1.33 \pm 0.014$	0.0	$2.19 \pm 0.027$	0.0	0.90	—	—	—
	N lobe	27.5	17.8	53.2	14.0	1.19	$0.84 \pm 0.02$	$-4 \pm 1$	6.85
	S lobe	32.8	7.3	62.2	5.2	1.15	$0.88 \pm 0.03$	$-24 \pm 3$	10.6
1217+36	'Core'	74.3	4.6	92.8	5.4	0.40	$1.13 \pm 0.02$	$10 \pm 2$	—
	Diffuse	36.4	7.4	70.0	3.5	1.18	$0.72 \pm 0.04$	$-9 \pm 5$	—
1256+36	NE lobe	35.8	9.9	63.6	10.3	1.03	$1.03 \pm 0.03$	$-13 \pm 2$	10 <sup>a</sup>
	SW lobe	60.5	11.2	108.2	9.9	1.04	$0.88 \pm 0.01$	$-3 \pm 1$	8 <sup>a</sup>
1257+36	'Core' NW	$0.13 \pm 0.012$	0.0	$0.11 \pm 0.026$	0.0	$-0.31 \pm 0.46$	—	—	—
	'Core' SE	$0.22 \pm 0.012$	0.0	$0.30 \pm 0.026$	0.0	$0.55 \pm 0.18$	—	—	—
	SE lobe	15.9	2.3	28.7	1.9	1.06	$0.99 \pm 0.03$	$35 \pm 2$	20.8
	NW lobe	22.9	12.0	42.4	10.9	1.11	$0.96 \pm 0.01$	$9 \pm 1$	18.2

<sup>a</sup> Based upon positions of optical IDs.

*1100 + 35* : The radio structure of this source strongly resembles that of a quasar, with a luminous flat-spectrum core, a bright one-sided jet leading to a compact lobe, and on the opposite side of the source a much more diffuse lobe closer to the nucleus (see also Law-Green et al. 1995). Lilly (1989) omitted this from his sample of radio galaxies on the basis of its bright infrared magnitude, and Law-Green et al. classified it as a quasar. However, no broad lines are seen in its optical spectrum (Rawlings et al. 1998; the signal-to-noise ratio of the spectrum is low, however, and so the limits set are not especially tight), and its infrared K-band emission is resolved (Figure 6h). 1100+35 should therefore be classified as a galaxy. Although strongly asymmetric in appearance and flux density, the two lobes of this radio source show little difference in their polarisation properties.

*1129 + 37* : No radio core is detected for this object in the current observations, although the host galaxy identification by Allington-Smith (1982) is secure and the galaxy has a redshift of 1.06 (Rawlings et al. 1998). The south-eastern lobe of the radio source contains three hotspots and is strongly polarised with a well-defined magnetic field structure. The hotspot closest to the nucleus corresponds to a region of significantly higher rotation measure than the two more distant hotspots, by as much as a few hundred rad m $^{-2}$  in the source rest-frame. The north-western lobe is more regular and has a lower polarisation.

*1204 + 35* : This source contains a strong radio core (see also Law-Green et al. 1995) which, although it has a relatively steep radio spectrum, is co-incident with the optical identification of Allington-Smith (1982). Rawlings et al.

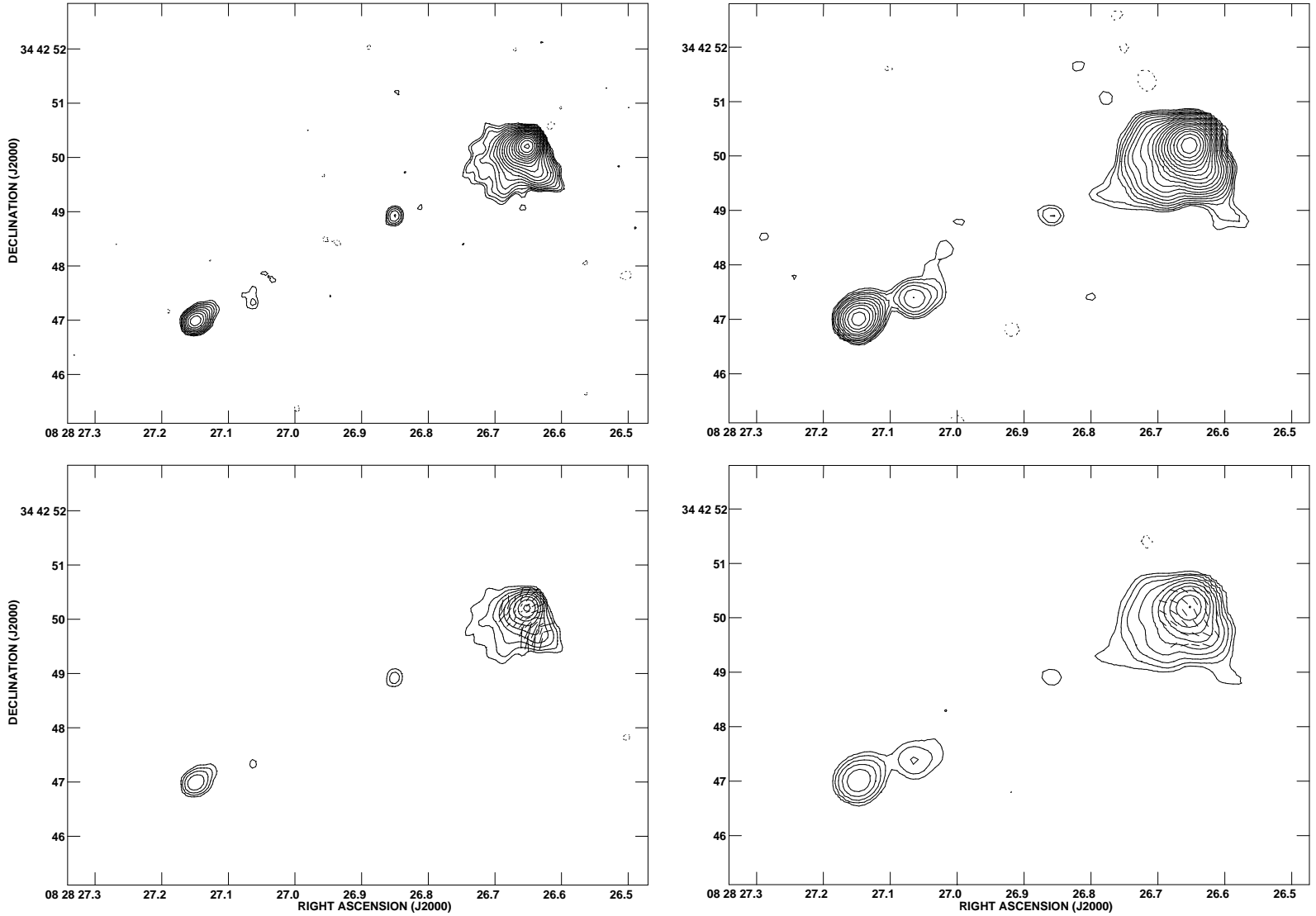


Figure 1: Maps of the radio source **0825+34**. (a – upper left) 8210 MHz total intensity map, FWHM 0.25 arcsec, with contours at  $60 \mu\text{Jy beam}^{-1} \times (-1, 1, 1.414, 2, 2.828, 4, \dots, 1024)$ . (b – upper right) 4710 MHz total intensity map, FWHM 0.4 arcsec, with contours at  $75 \mu\text{Jy beam}^{-1} \times (-1, 1, 1.414, 2, 2.828, 4, \dots, 1024)$ . (c – lower left) The 8210 MHz radio map with vectors of polarisation overlaid. A vector of length 1.2 arcsec corresponds to 100% polarisation. The contour levels are  $80 \mu\text{Jy beam}^{-1} \times (-1, 1, 2, 4, \dots, 1024)$ . (d – lower right) The magnetic field position angle, plotted wherever a rotation measure could be calculated.

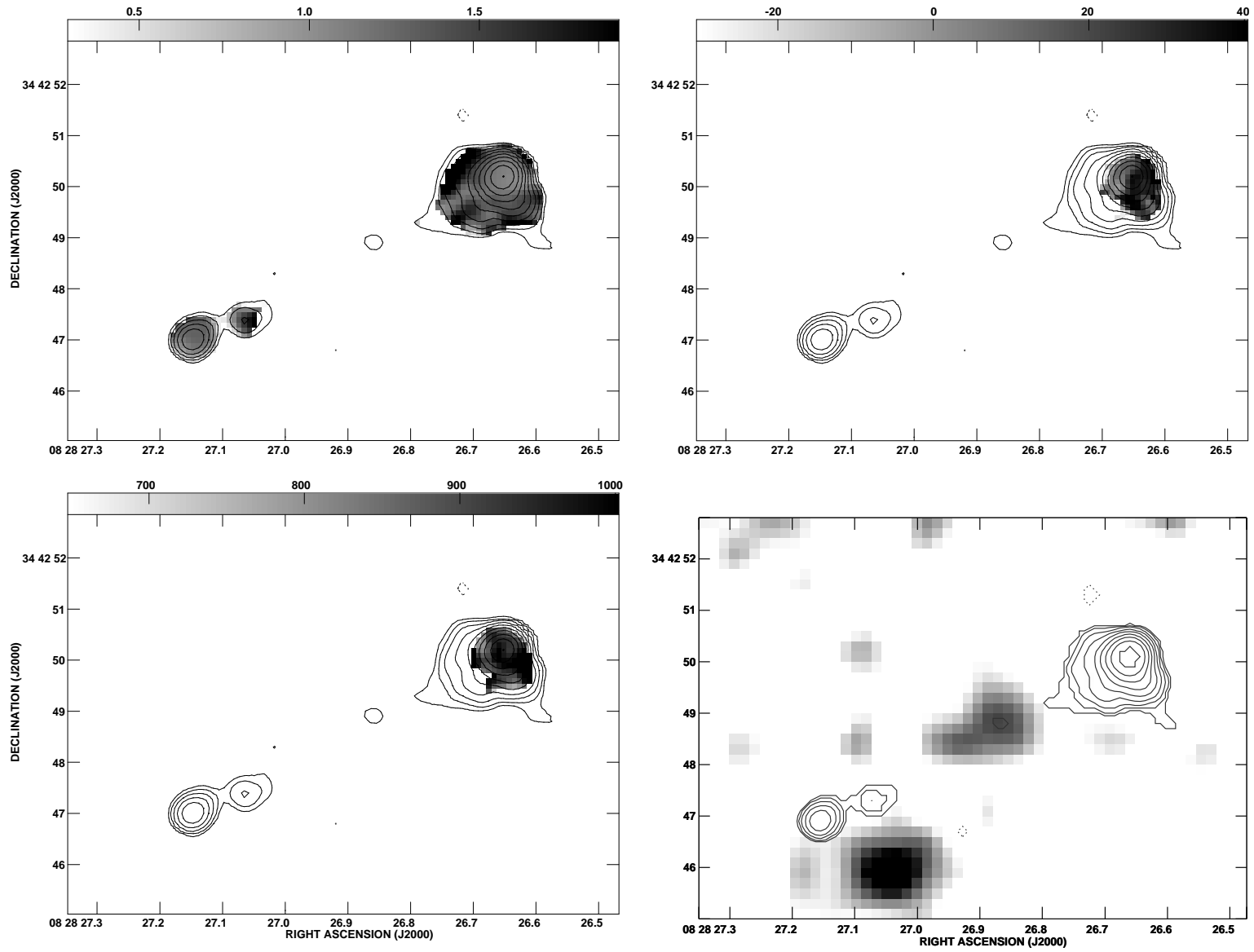


Figure 1: **cont.** (e – upper left) A spectral index map of the source, calculated between the frequencies 4710 and 8210 MHz. (f – upper right) A rotation measure map of the source, calculated from the frequencies 4535, 4885 and 8210 MHz. (g – lower left) A map of the depolarisation measure between 8210 and 4710 MHz (units in milli-ratios). (h – lower right) The 48–minute infrared K–band image taken using IRCAM of UKIRT. The contours of radio emission at 4710 MHz overlaid on figures (d) through to (h) are at  $100 \mu\text{Jy beam}^{-1} \times (-1, 1, 2, 4, \dots, 1024)$ .

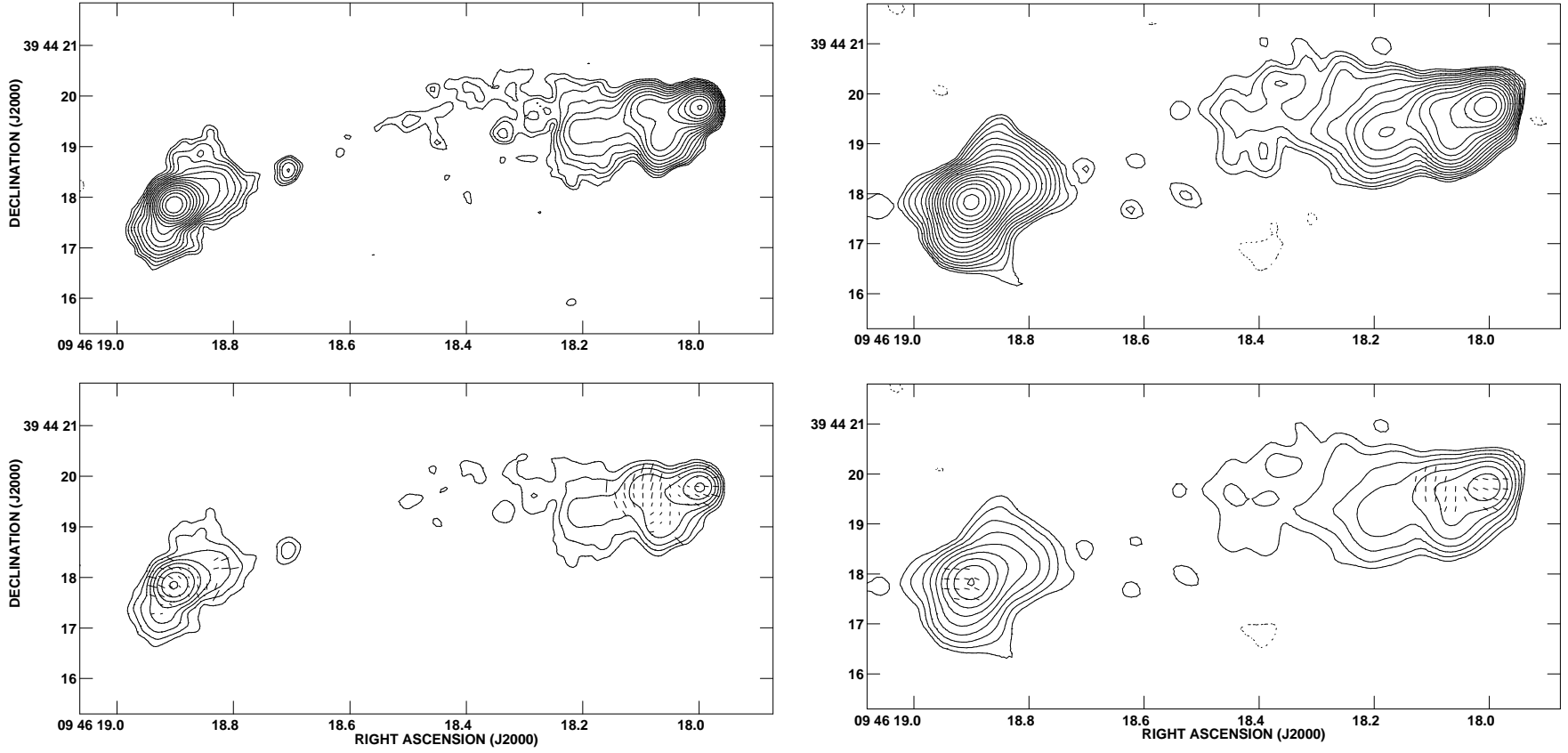


Figure 2: Maps of the radio source **0943+39**. (a – upper left) 8210 MHz total intensity map, FWHM 0.35 arcsec, with contours at  $50 \mu\text{Jy beam}^{-1} \times (-1, 1, 1.414, 2, 2.828, 4, \dots, 1024)$ . (b – upper right) 4710 MHz total intensity map, FWHM 0.55 arcsec, with contours at  $80 \mu\text{Jy beam}^{-1} \times (-1, 1, 1.414, 2, 2.828, 4, \dots, 1024)$ . (c – lower left) The 8210 MHz radio map with vectors of polarisation overlaid. A vector of length 0.6 arcsec corresponds to 100% polarisation. The contour levels are  $65 \mu\text{Jy beam}^{-1} \times (-1, 1, 2, 4, \dots, 1024)$ . (d – lower right) The magnetic field position angle, plotted wherever a rotation measure could be calculated.



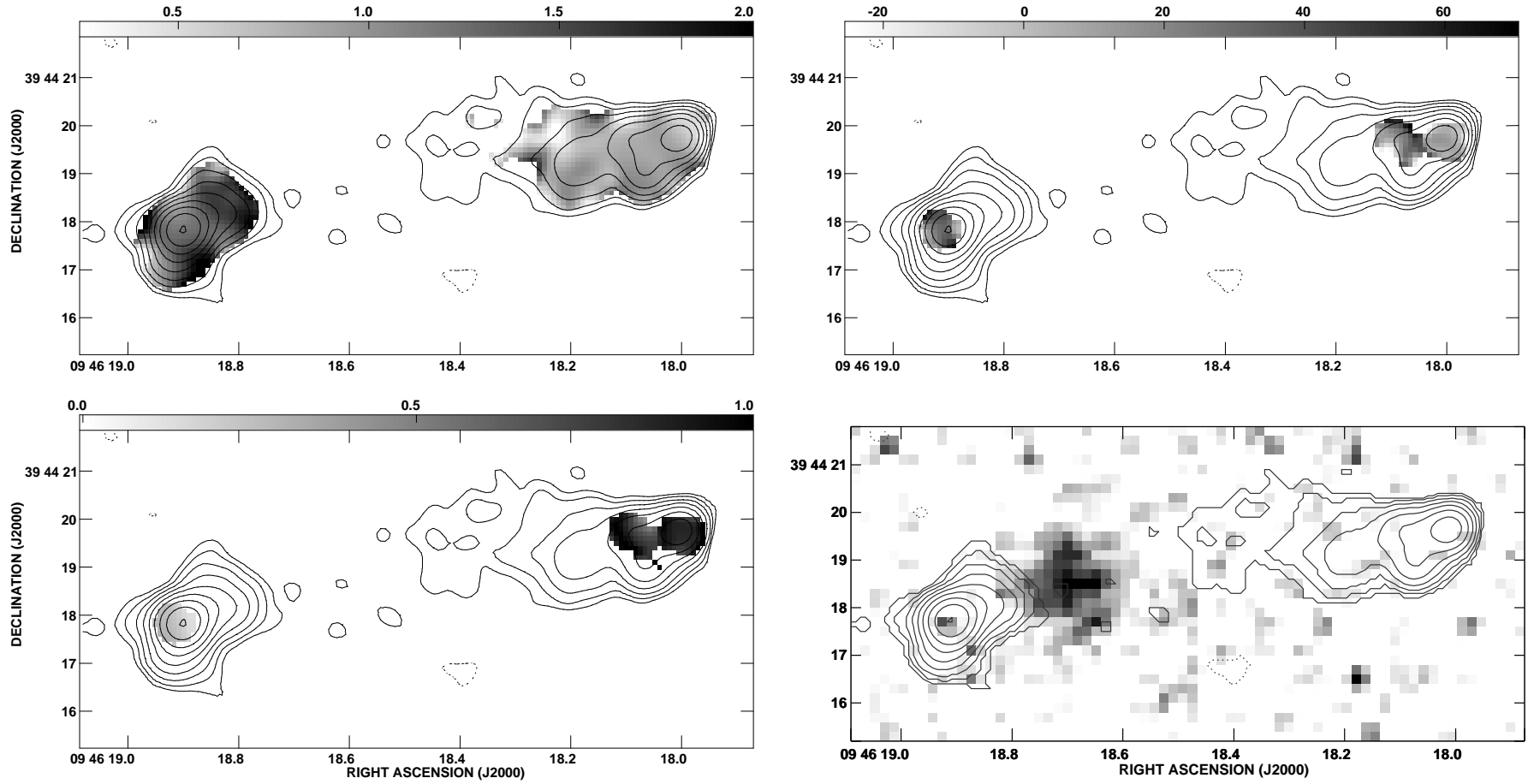


Figure 2: **cont.** (e – upper left) A spectral index map of the source, calculated between the frequencies 4710 and 8210 MHz. (f – upper right) A rotation measure map of the source, calculated from the frequencies 4535, 4885 and 8210 MHz. (g – lower left) A map of the depolarisation measure between 8210 and 4710 MHz. (h – lower right) The 27-minute infrared K-band image taken using IRCAM3 of UKIRT. The contours of radio emission at 4710 MHz overlaid on figures (d) through to (h) are at  $90\mu\text{Jy beam}^{-1} \times (-1, 1, 2, 4 \dots 1024)$ .

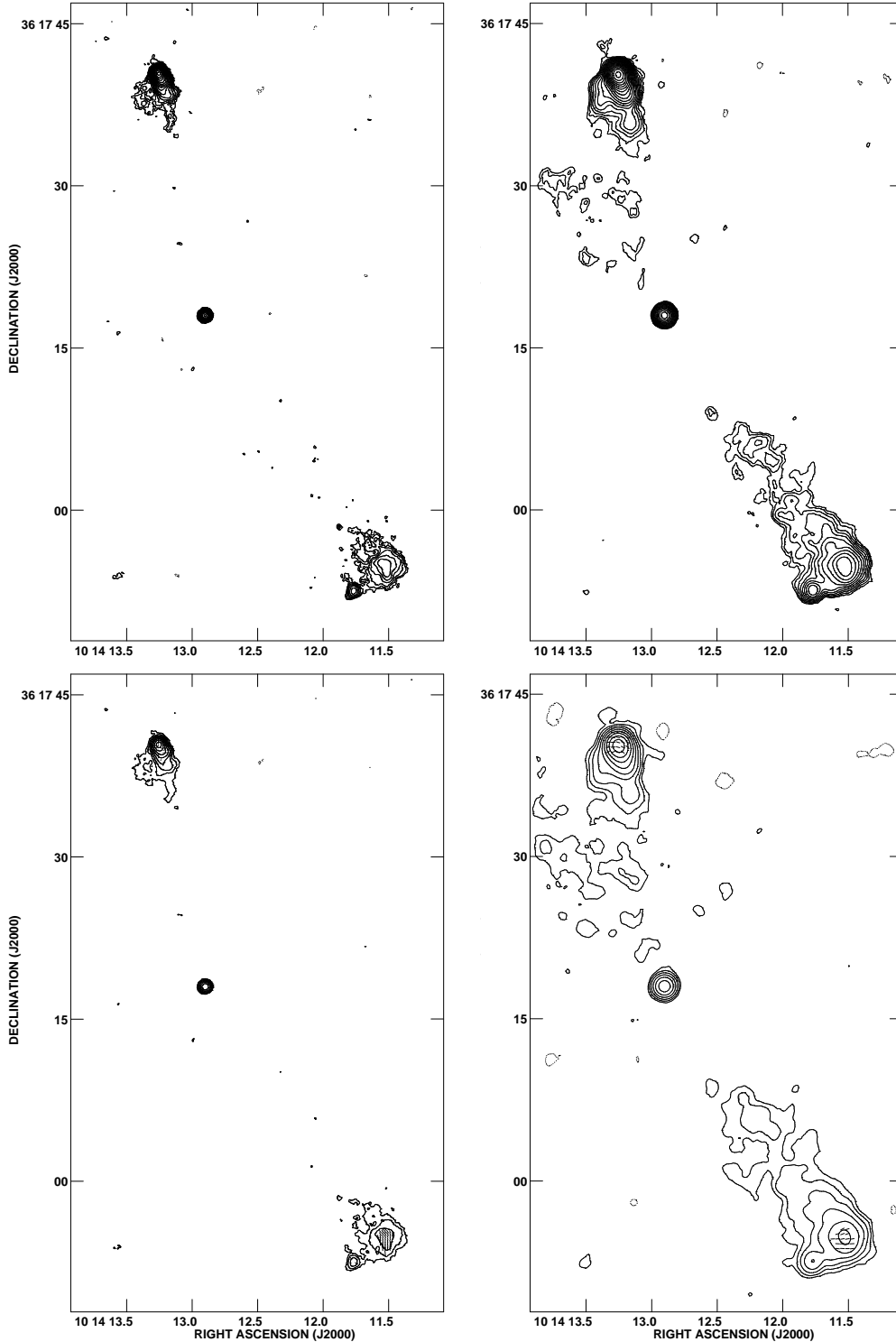


Figure 3: Maps of the radio source **1011+36**. (a – upper left) 8210 MHz total intensity map, FWHM 0.6 arcsec, with contours at  $70\mu\text{Jy beam}^{-1} \times (-1, 1, 1.414, 2, 2.828, 4 \dots 1024)$ . (b – upper right) 4710 MHz total intensity map, FWHM 1.0 arcsec, with contours at  $70\mu\text{Jy beam}^{-1} \times (-1, 1, 1.414, 2, 2.828, 4 \dots 1024)$ . (c – lower left) The 8210 MHz radio map with vectors of polarisation overlaid. A vector of length 1.20 arcsec corresponds to 100% polarisation. The contour levels are at  $90\mu\text{Jy beam}^{-1} \times (-1, 1, 2, 4 \dots 1024)$ . (d – lower right) The magnetic field position angle, plotted wherever a rotation measure could be calculated.

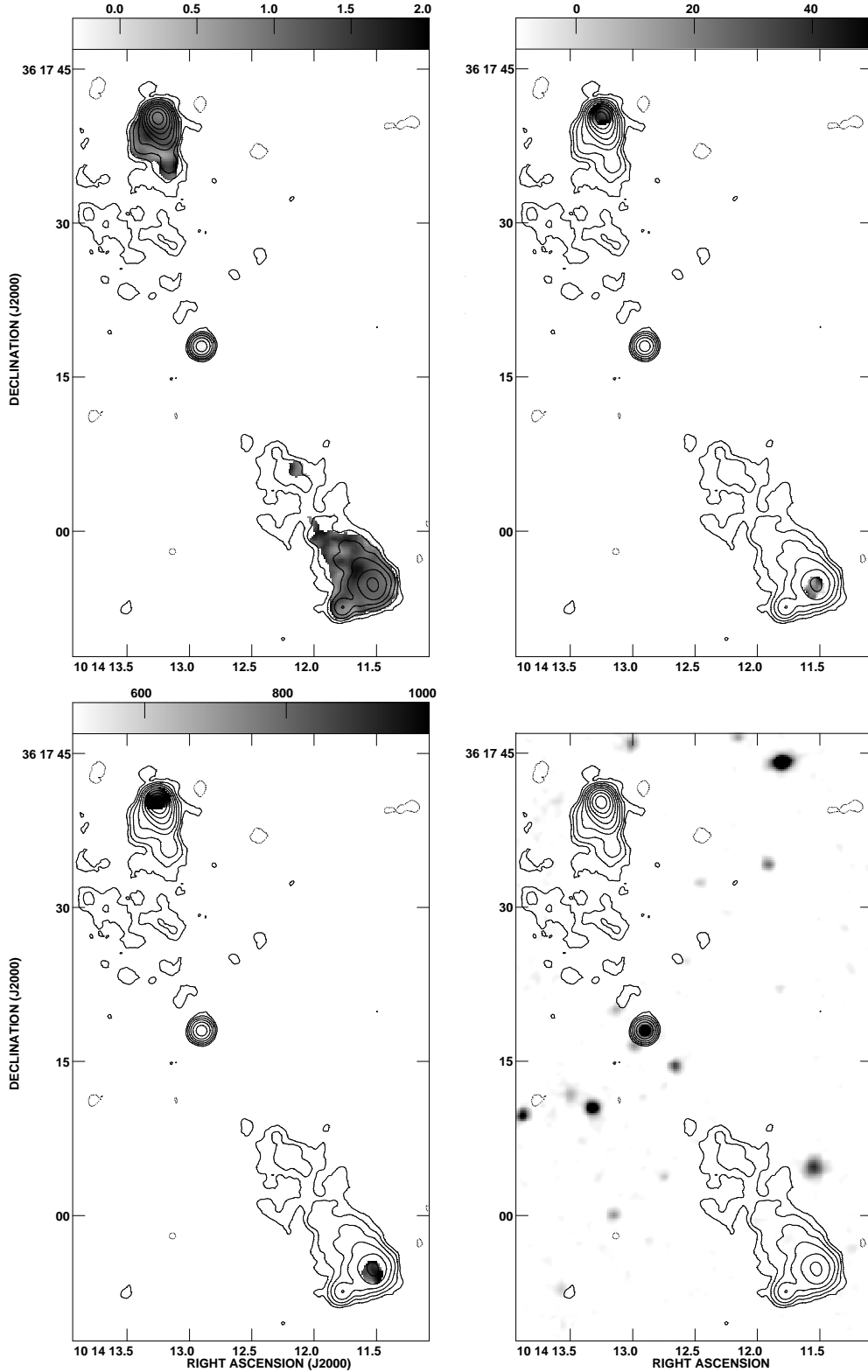


Figure 3: **cont.** (e – upper left) A spectral index map of the source, calculated between the frequencies 4710 and 8210 MHz. (f – upper right) A rotation measure map of the source, calculated from the frequencies 4535, 4885 and 8210 MHz. (g – lower left) A map of the depolarisation measure between 8210 and 4710 MHz (units in milli-ratios). (h – lower right) The 45-minute infrared K-band image taken using the REDEYE camera on the CFHT. The radio maps at 8210 MHz overlaid on figures (d) through to (h) have FWHM 1.25 arcsec and contours at  $80\mu\text{Jy beam}^{-1} \times (-1, 1, 2, 4, \dots, 1024)$ .

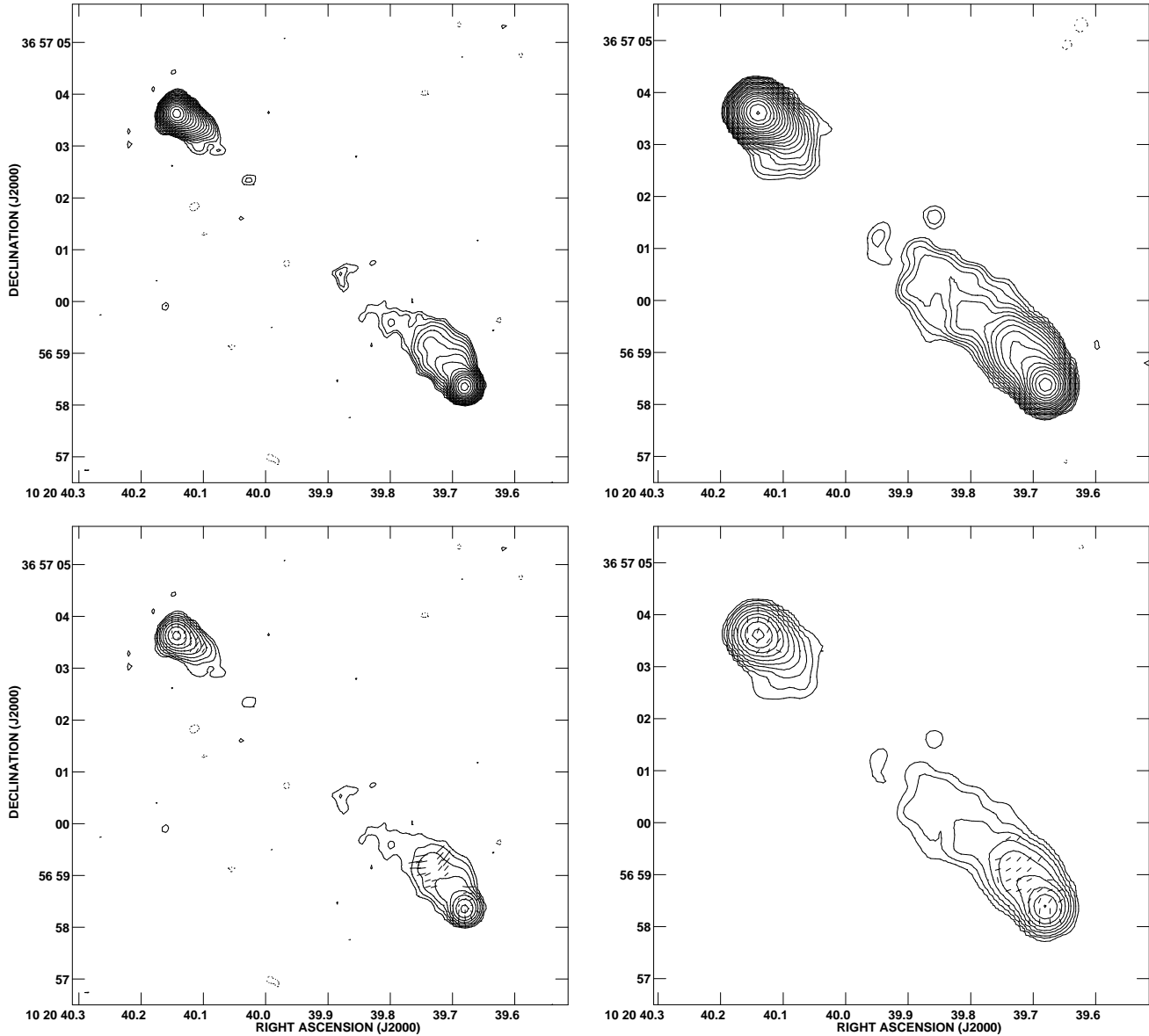


Figure 4: Maps of the radio source **1017+37**. (a – upper left) 8210 MHz total intensity map, FWHM 0.25 arcsec, with contours at  $65\mu\text{Jy beam}^{-1} \times (-1, 1, 1.414, 2, 2.828, 4 \dots 1024)$ . (b – upper right) 4710 MHz total intensity map, FWHM 0.4 arcsec, with contours at  $65\mu\text{Jy beam}^{-1} \times (-1, 1, 1.414, 2, 2.828, 4 \dots 1024)$ . (c – lower left) The 8210 MHz radio map with vectors of polarisation overlaid. A vector of length 0.48 arcsec corresponds to 100% polarisation. The contour levels are  $65\mu\text{Jy beam}^{-1} \times (-1, 1, 2, 4 \dots 1024)$ . (d – lower right) The magnetic field position angle, plotted wherever a rotation measure could be calculated.

(1998) have determined the redshift of the host galaxy to be  $z = 1.37$ . Both radio lobes contain double hotspots and show moderate depolarisation.

*1217 + 36* : This source has a very peculiar radio morphology (see also Naundorf et al. 1992; Law-Green et al. 1995). A central compact double, 0.7 arcsec in extent, is surrounded by an halo of emission extending more than 4 arcsecs. The spectral index of this radio halo steepens with distance out from the central object; if we had not restricted the spectral index map to regions where flux was detected at greater than the 5-sigma level in both maps, then it could

have been seen to steepen to values of 2.5 or more in the outer regions of the halo. The north-eastern of the two compact emission knots has a relatively flat spectral index and probably includes the radio core, but the brightness of this region, its resolved size, and the detection of polarised emission from it suggests that this knot does not contain solely the radio core. Also interesting is that the region of flattest spectral index appears to be offset by about 0.5 arcsec east from the peak of the radio flux density.

The emission from the central region of this source shows no depolarisation, which is surprising given that this

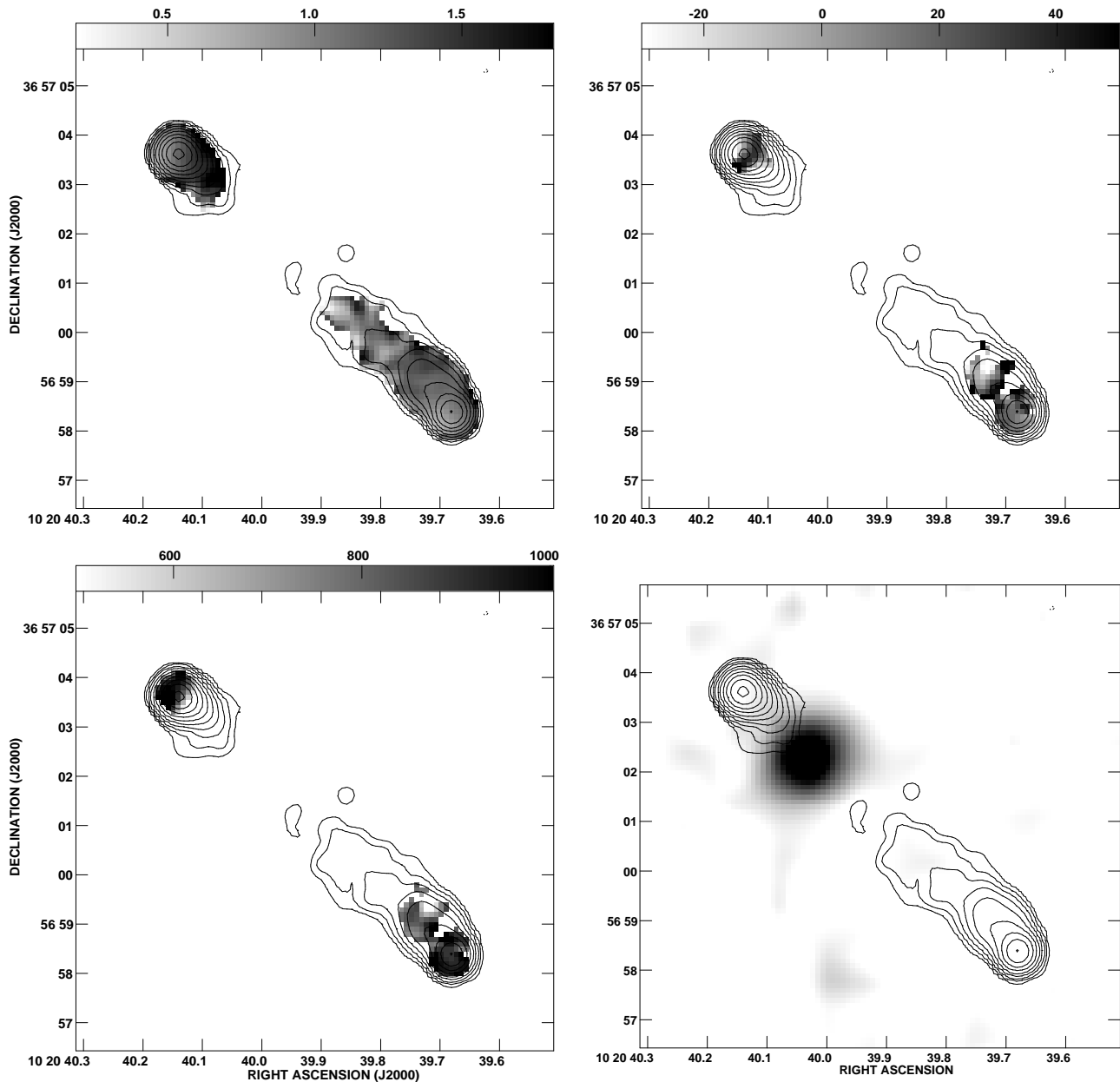


Figure 4: **cont.** (e – upper left) A spectral index map of the source, calculated between the frequencies 4710 and 8210 MHz. (f – upper right) A rotation measure map of the source, calculated from the frequencies 4535, 4885 and 8210 MHz. (g – lower left) A map of the depolarisation measure between 8210 and 4710 MHz (units in milli-ratios). (h – lower right) The 26-minute infrared K-band image taken using the REDEYE camera on the CFHT. The contours of radio emission at 4710 MHz overlaid on figures (d) through to (h) are at  $80 \mu\text{Jy beam}^{-1} \times (-1, 1, 2, 4 \dots 1024)$ .

should lie well within the gas of the host galaxy. The diffuse emission halo is more strongly depolarised. There is also a steep gradient in the rotation measure across the source.

Benítez et al. (1995) suggested that this galaxy was stellar-like on their R-band image. They therefore proposed that it should perhaps be reclassified as a quasar and that the redshift of 1.2 estimated from its K-magnitude (Lilly 1989) would be too high. A spectrum by Rawlings et al. (1998) has provided a redshift of  $z = 1.09$ , close to Lilly's

estimate (although based upon only one emission line). Neither this spectrum nor the K-band image suggest that this source is a quasar.

*1256 + 36*: This radio source was identified by Lilly (1989) with a galaxy whose redshift has been determined as  $z = 1.07$  (Rawlings et al. 1998). Although no radio core is detected on our radio maps, the identification is secure, lies directly between the two radio lobes, and appears to show

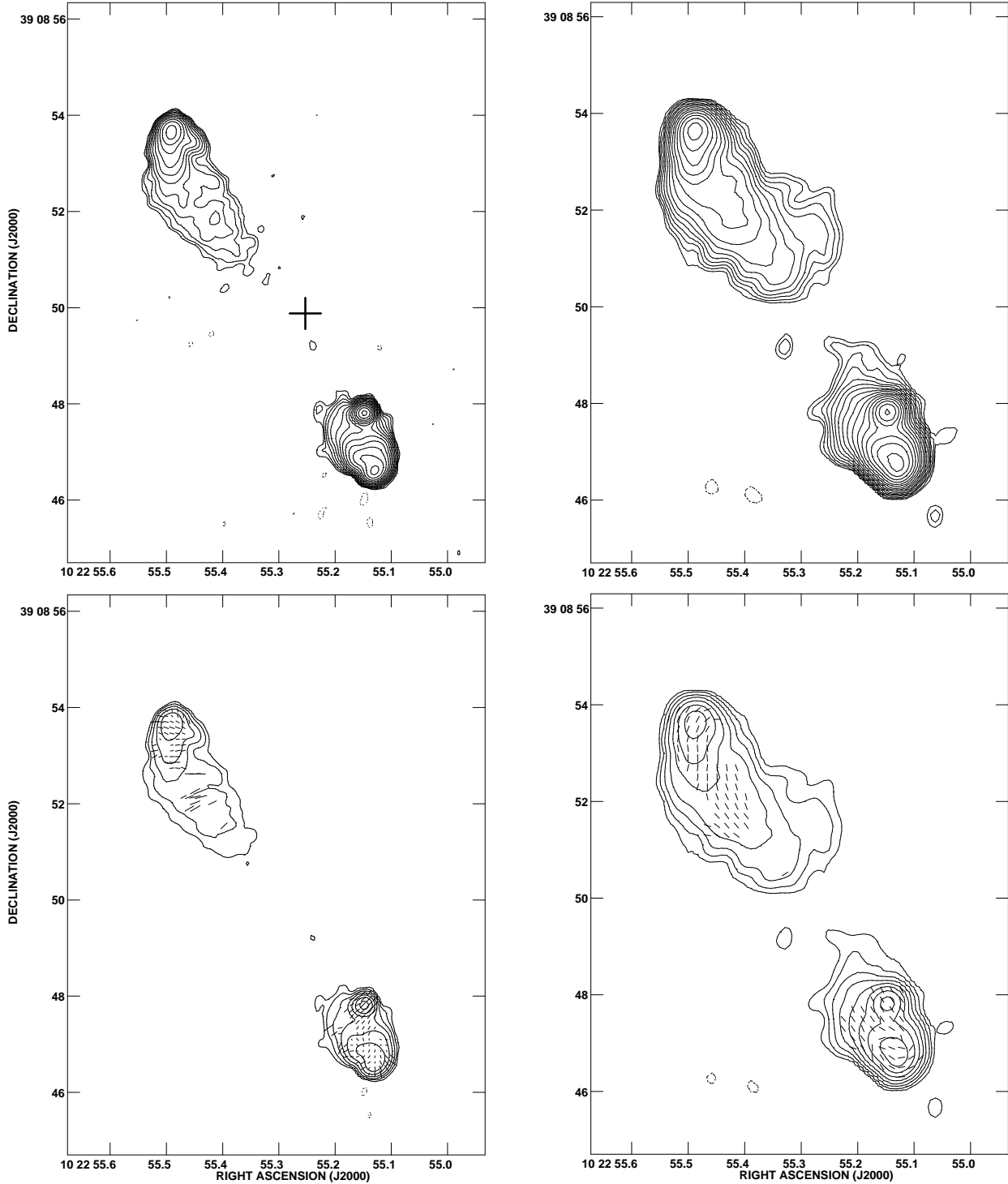


Figure 5: Maps of the radio source **1019+39**. (a – upper left) 8210 MHz total intensity map, FWHM 0.25 arcsec, with contours at  $75\mu\text{Jy beam}^{-1} \times (-1, 1, 1.414, 2, 2.828, 4 \dots 1024)$ . The cross marks the position of the optical host galaxy. (b – upper right) 4710 MHz total intensity map, FWHM 0.4 arcsec, with contours at  $80\mu\text{Jy beam}^{-1} \times (-1, 1, 1.414, 2, 2.828, 4 \dots 1024)$ . (c – lower left) The 8210 MHz radio map with vectors of polarisation overlaid. A vector of length 0.6 arcsec corresponds to 100% polarisation. The contour levels are  $90\mu\text{Jy beam}^{-1} \times (-1, 1, 2, 4 \dots 1024)$ . (d – lower right) The magnetic field position angle, plotted wherever a rotation measure could be calculated.

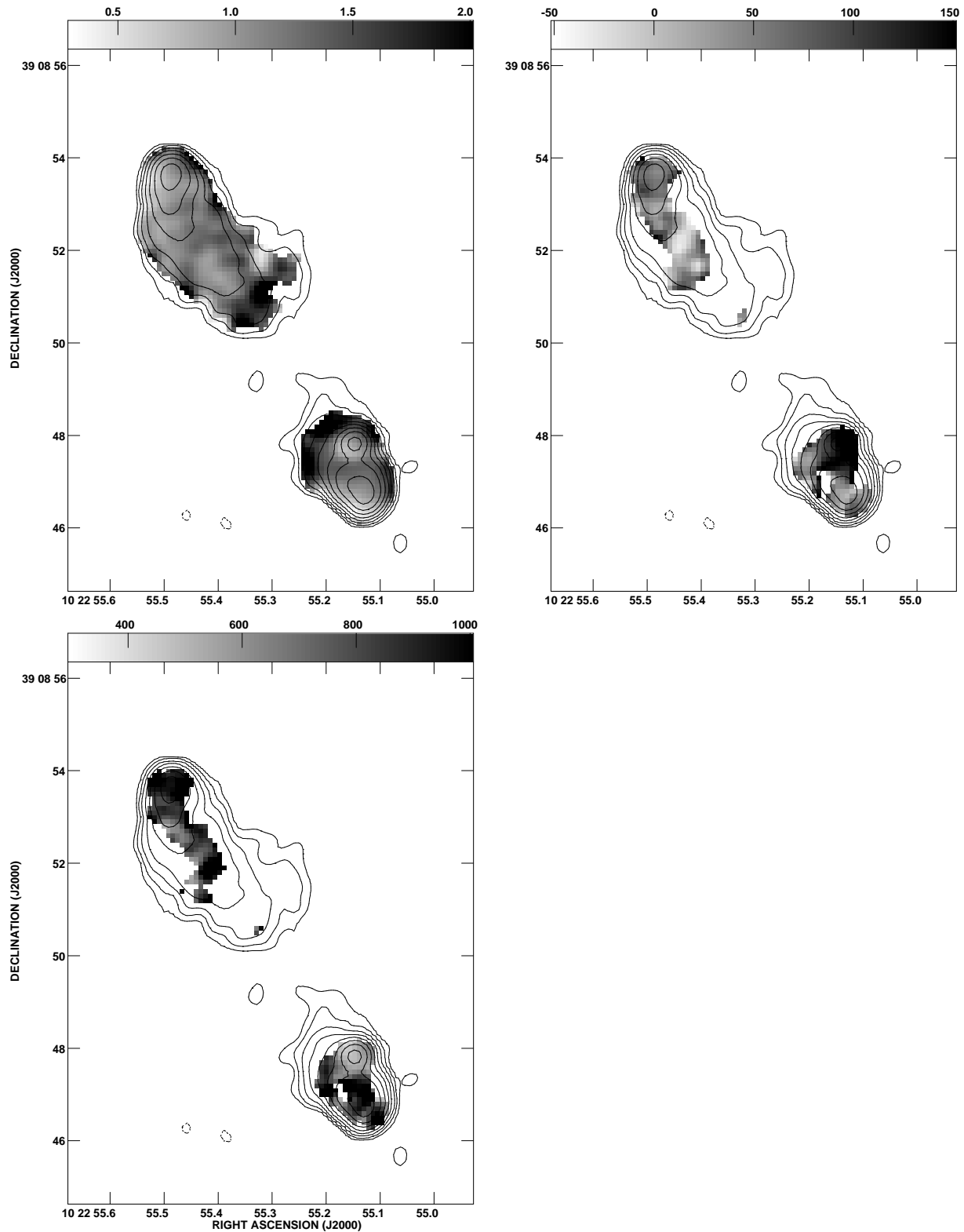


Figure 5: **cont.** (e – upper left) A spectral index map of the source, calculated between the frequencies 4710 and 8210 MHz. (f – upper right) A rotation measure map of the source, calculated from the frequencies 4535, 4885 and 8210 MHz. (g – lower left) A map of the depolarisation measure between 8210 and 4710 MHz (units in milli-ratios). The contours of radio emission at 4710 MHz overlaid on figures (d) through to (g) are at  $90 \mu\text{Jy beam}^{-1} \times (-1, 1, 2, 4, \dots, 1024)$ .

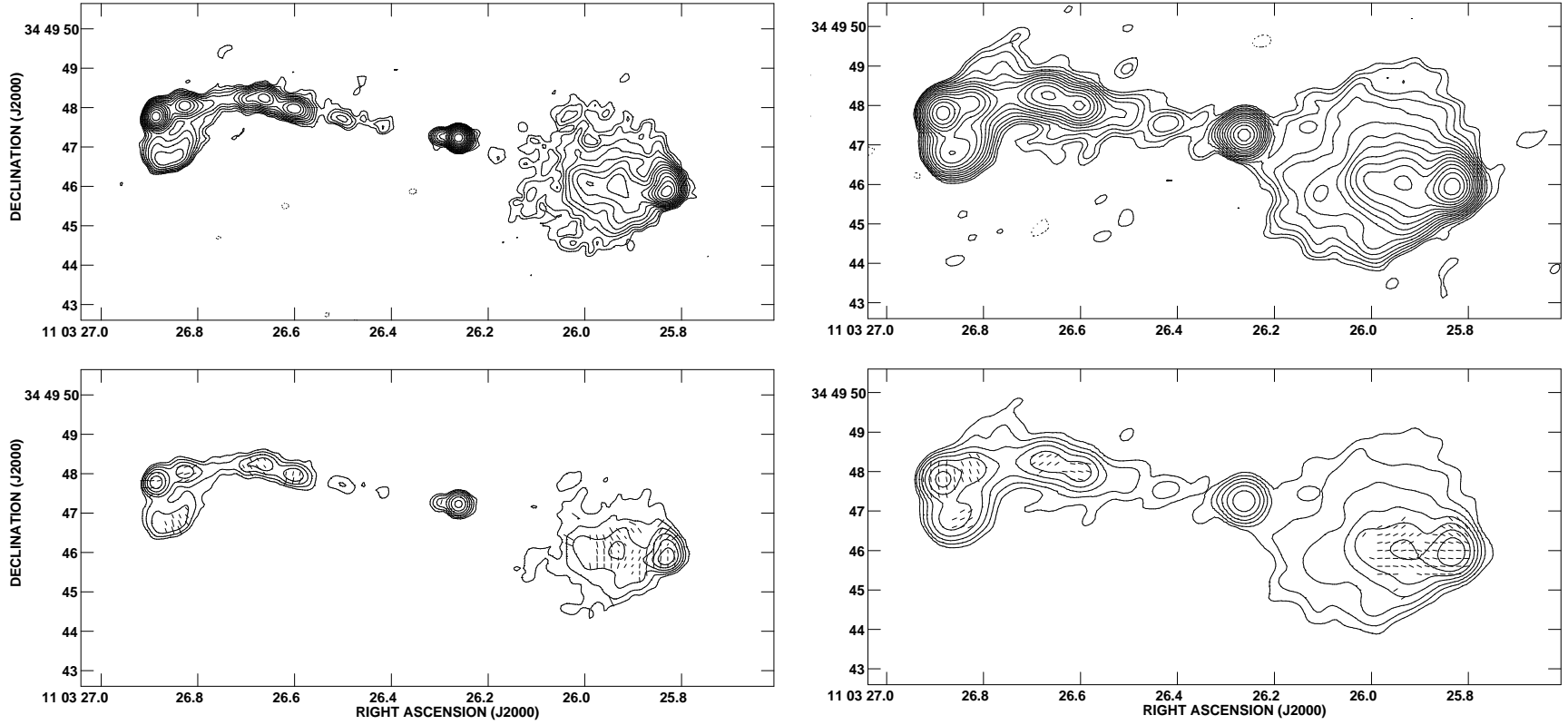


Figure 6: Maps of the radio source **1100+35**. (a – upper left) 8210 MHz total intensity map, FWHM 0.3 arcsec, with contours at  $50 \mu\text{Jy beam}^{-1} \times (-1, 1, 1.414, 2, 2.828, 4, \dots, 1024)$ . (b – upper right) 4710 MHz total intensity map, FWHM 0.55 arcsec, with contours at  $75 \mu\text{Jy beam}^{-1} \times (-1, 1, 1.414, 2, 2.828, 4, \dots, 1024)$ . (c – lower left) The 8210 MHz radio map with vectors of polarisation overlaid. A vector of length 0.6 arcsec corresponds to 100% polarisation. The contour levels are  $75 \mu\text{Jy beam}^{-1} \times (-1, 1, 2, 4, \dots, 1024)$ . (d – lower right) The magnetic field position angle, plotted wherever a rotation measure could be calculated.



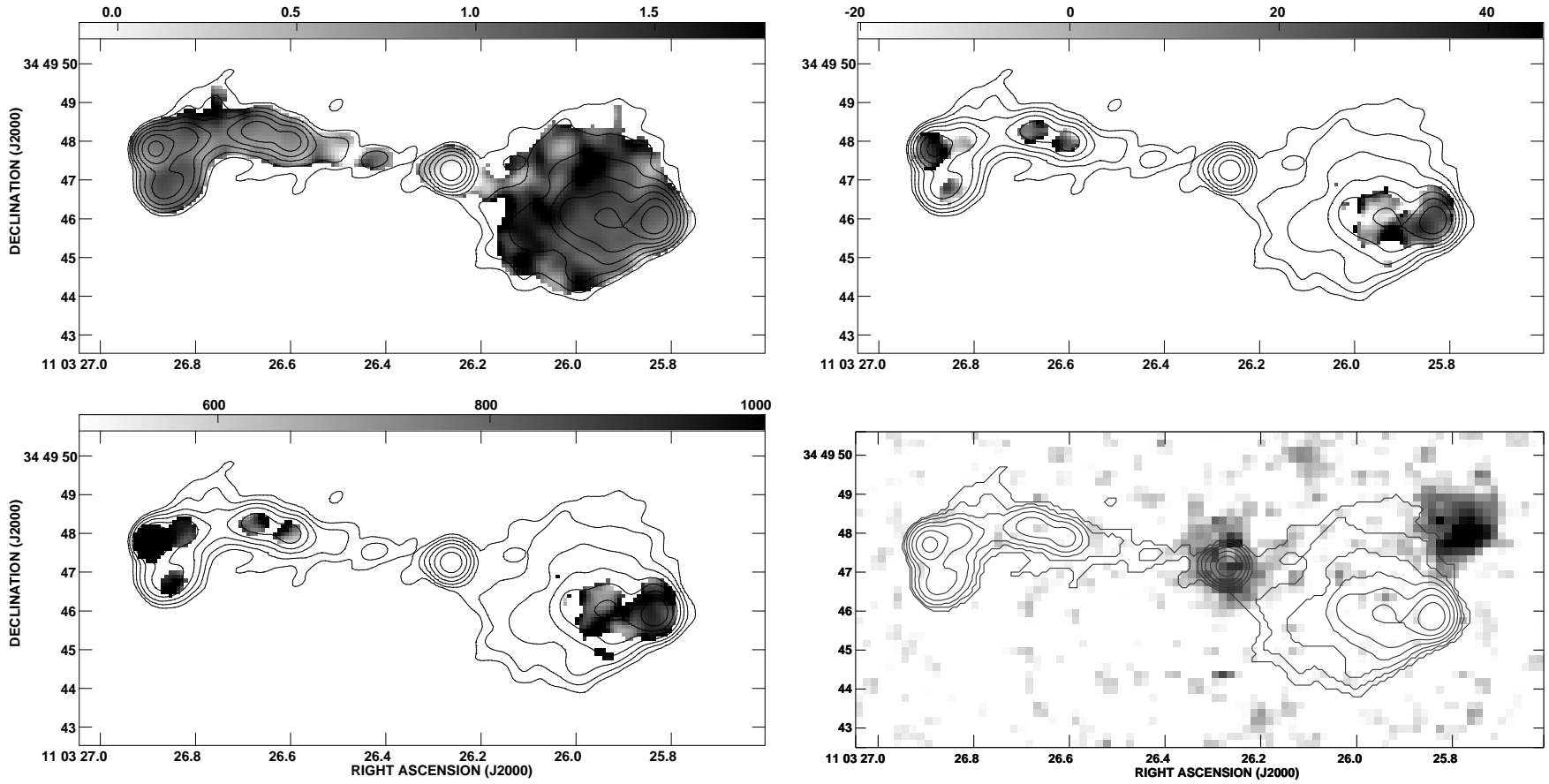


Figure 6: **cont.** (e – upper left) A spectral index map of the source, calculated between the frequencies 4710 and 8210 MHz. (f – upper right) A rotation measure map of the source, calculated from the frequencies 4535, 4885 and 8210 MHz. (g – lower left) A map of the depolarisation measure between 8210 and 4710 MHz (units in milli-ratios). (h – lower right) The 18-minute infrared K-band image taken using IRCAM3 on UKIRT. The contours of radio emission at 4710 MHz overlaid on figures (d) through to (h) are at  $100\mu\text{Jy beam}^{-1} \times (-1, 1, 2, 4 \dots 1024)$ .

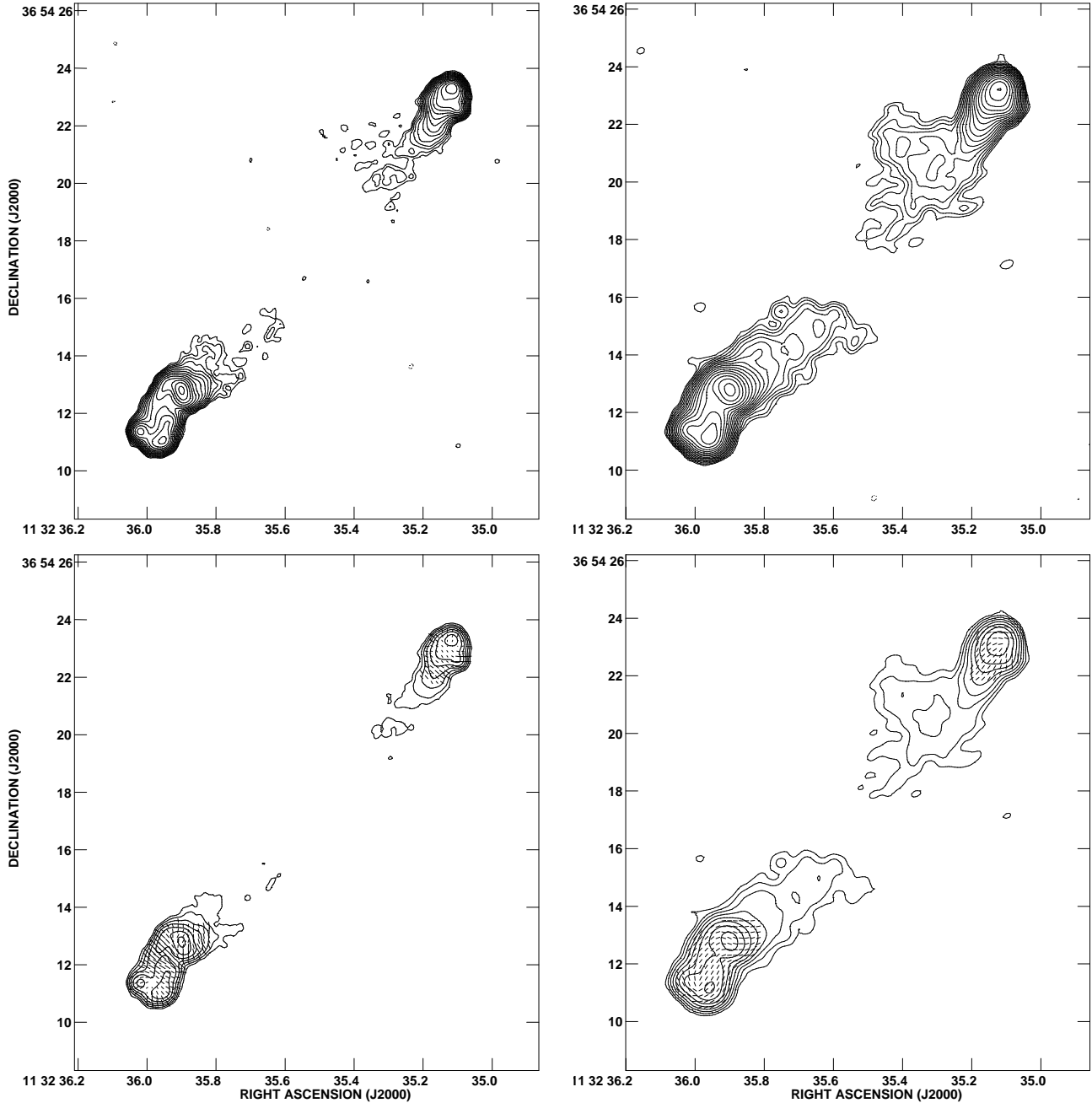


Figure 7: Maps of the radio source **1129+37**. (a – upper left) 8210 MHz total intensity map, FWHM 0.35 arcsec, with contours at  $45\mu\text{Jy beam}^{-1} \times (-1, 1, 1.414, 2, 2.828, 4 \dots 1024)$ . (b – upper right) 4710 MHz total intensity map, FWHM 0.55 arcsec, with contours at  $60\mu\text{Jy beam}^{-1} \times (-1, 1, 1.414, 2, 2.828, 4 \dots 1024)$ . (c – lower left) The 8210 MHz radio map with vectors of polarisation overlaid. A vector of length 0.6 arcsec corresponds to 100% polarisation. The contour levels are  $60\mu\text{Jy beam}^{-1} \times (-1, 1, 2, 4 \dots 1024)$ . (d – lower right) The magnetic field position angle, plotted wherever a rotation measure could be calculated.

an elongation along the radio axis. Lilly (1989) detected five other galaxies within a few arcseconds of the host, possibly forming the core of a rich group or cluster; only two of these are detected in our (albeit slightly shallower) K-band image. The hotspot in the south-western radio lobe is withdrawn from the leading edge of the emission (see also Law-

Green et al. 1995). The two lobes show only small variations between their spectral indices, depolarisation and rotation measures.

*1257 + 36* : Two core candidates, separated by only 1.5 arcseconds, lie towards the centre of this radio source and close to the host galaxy identified by Eales et al. (1997) at

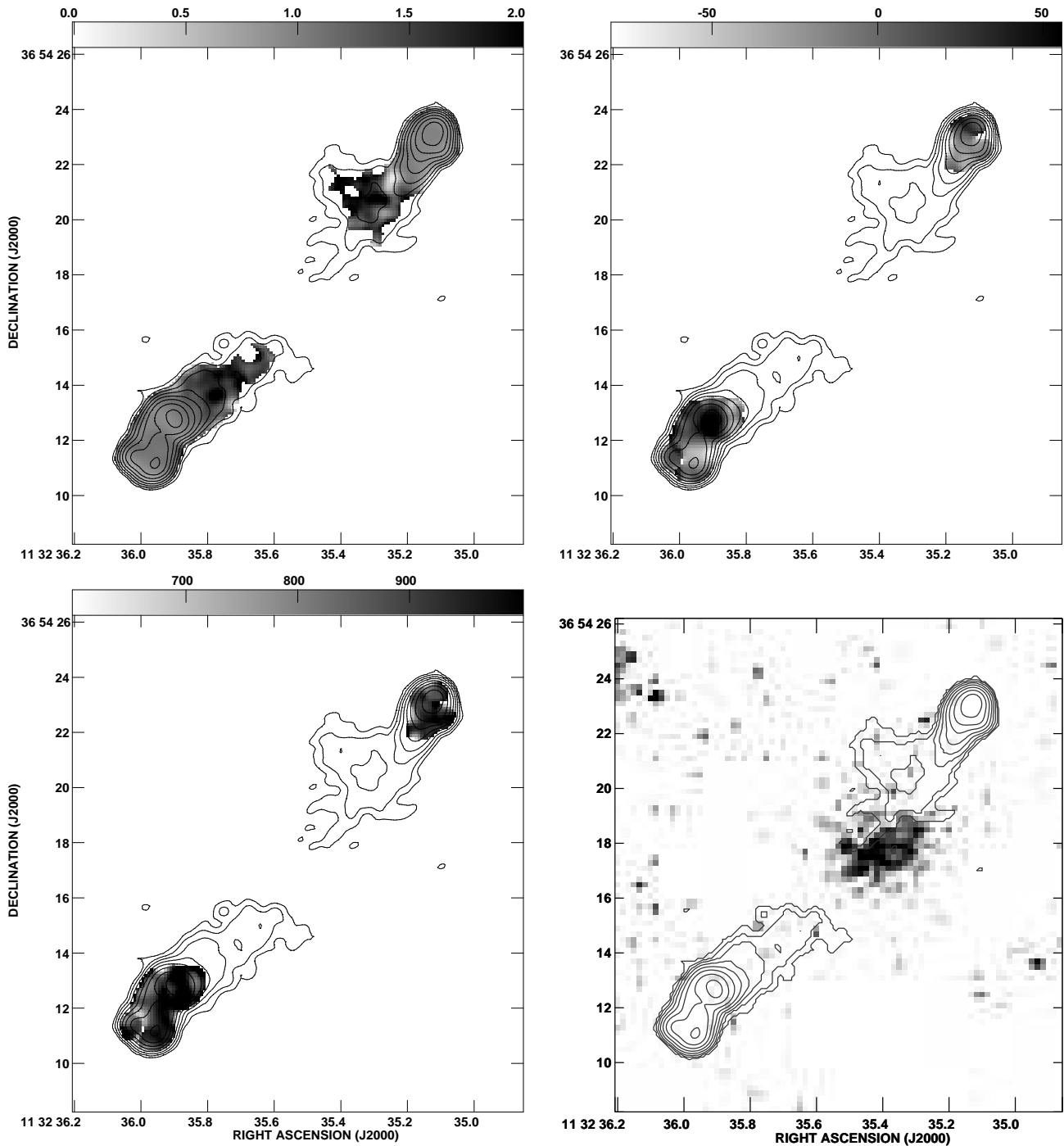


Figure 7: **cont.** (e – upper left) A spectral index map of the source, calculated between the frequencies 4710 and 8210 MHz. (f – upper right) A rotation measure map of the source, calculated from the frequencies 4535, 4885 and 8210 MHz. (g – lower left) A map of the depolarisation measure between 8210 and 4710 MHz (units in milli-ratios). (h – lower right) The 27-minute infrared K-band image taken using IRCAM3 on UKIRT. The contours of radio emission at 4710 MHz overlaid on figures (d) through to (h) are at  $70 \mu\text{Jy beam}^{-1} \times (-1, 1, 2, 4 \dots 1024)$ .

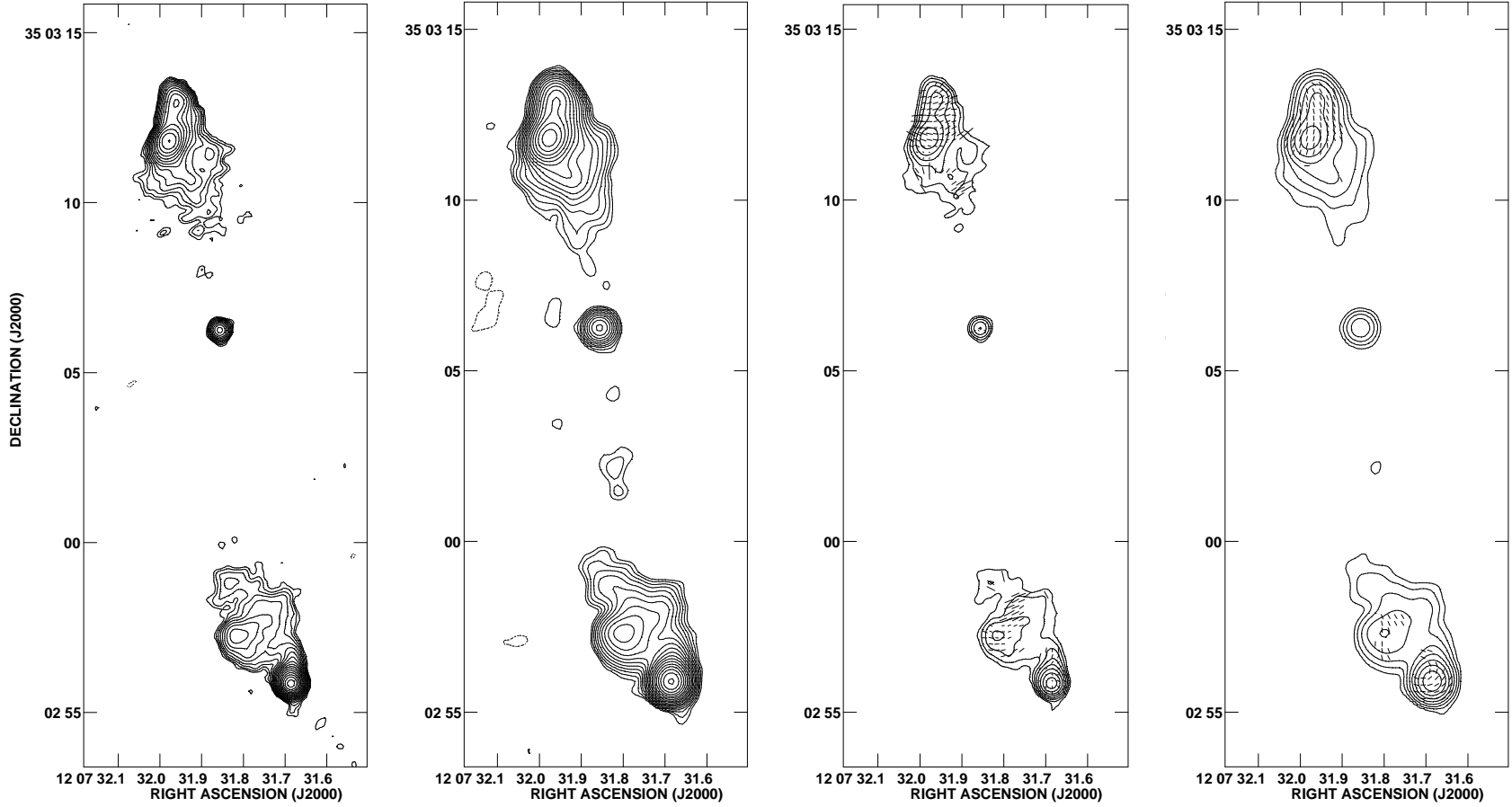


Figure 8: Maps of the radio source **1204+35**. (a – left) 8210 MHz total intensity map, FWHM 0.3 arcsec, with contours at  $50 \mu\text{Jy beam}^{-1} \times (-1, 1, 1.414, 2, 2.828, 4, \dots, 1024)$ . (b – centre left) 4710 MHz total intensity map, FWHM 0.55 arcsec, with contours at  $90 \mu\text{Jy beam}^{-1} \times (-1, 1, 1.414, 2, 2.828, 4, \dots, 1024)$ . (c – centre right) The 8210 MHz radio map with vectors of polarisation overlaid. A vector of length 0.6 arcsec corresponds to 100% polarisation. The contour levels are  $80 \mu\text{Jy beam}^{-1} \times (-1, 1, 2, 4, \dots, 1024)$ . (d – right) The magnetic field position angle, plotted wherever a rotation measure could be calculated.

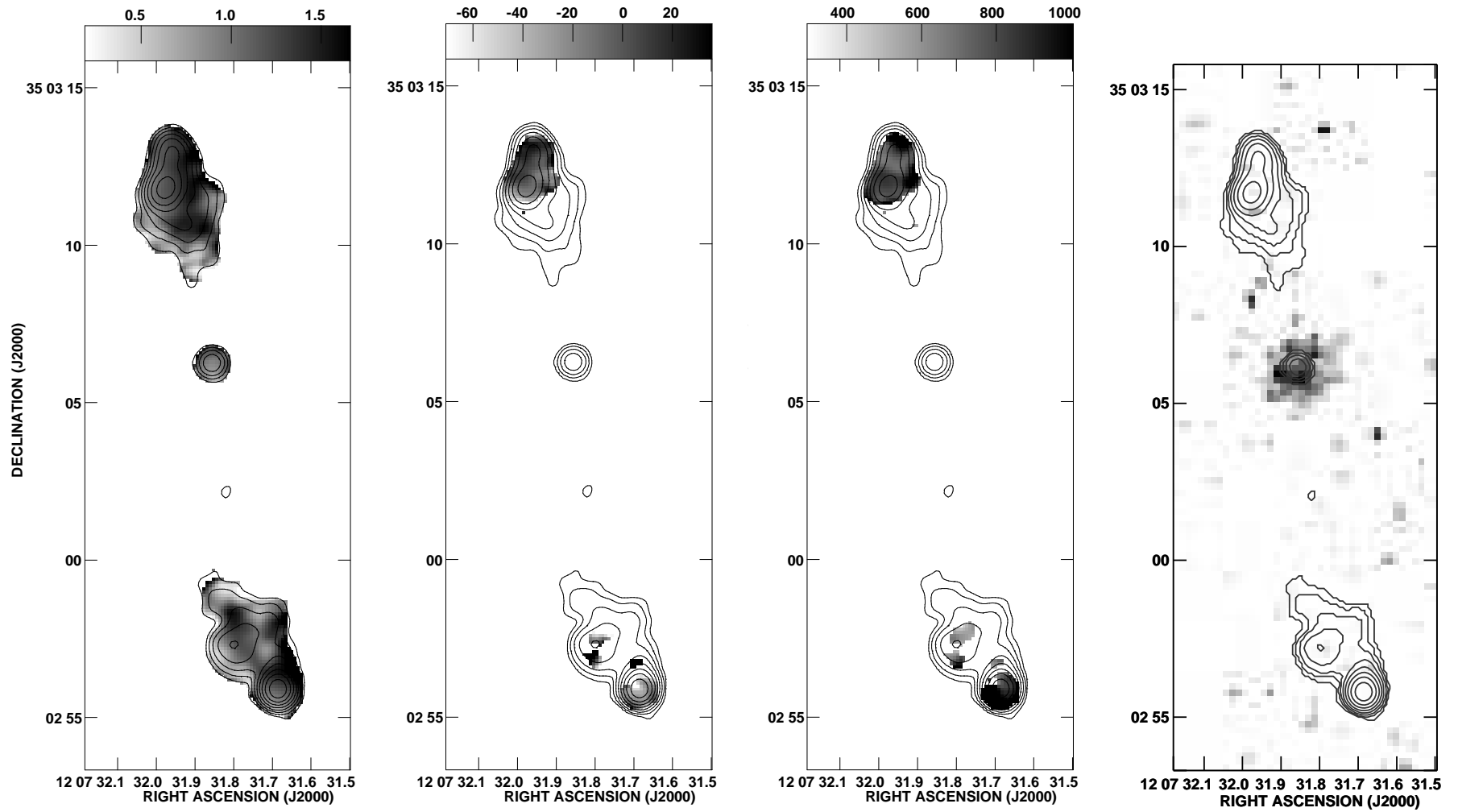


Figure 8: **cont.** (e – left) A spectral index map of the source, calculated between the frequencies 4710 and 8210 MHz. (f – centre left) A rotation measure map of the source, calculated from the frequencies 4535, 4885 and 8210 MHz. (g – centre right) A map of the depolarisation measure between 8210 and 4710 MHz (units in milli-ratios). (h – right) The 27-minute infrared K-band image taken using IRCAM3 of UKIRT. The contours of radio emission at 4710 MHz overlaid on figures (d) through to (h) are at  $150\mu\text{Jy beam}^{-1} \times (-1, 1, 2, 4 \dots 1024)$ .

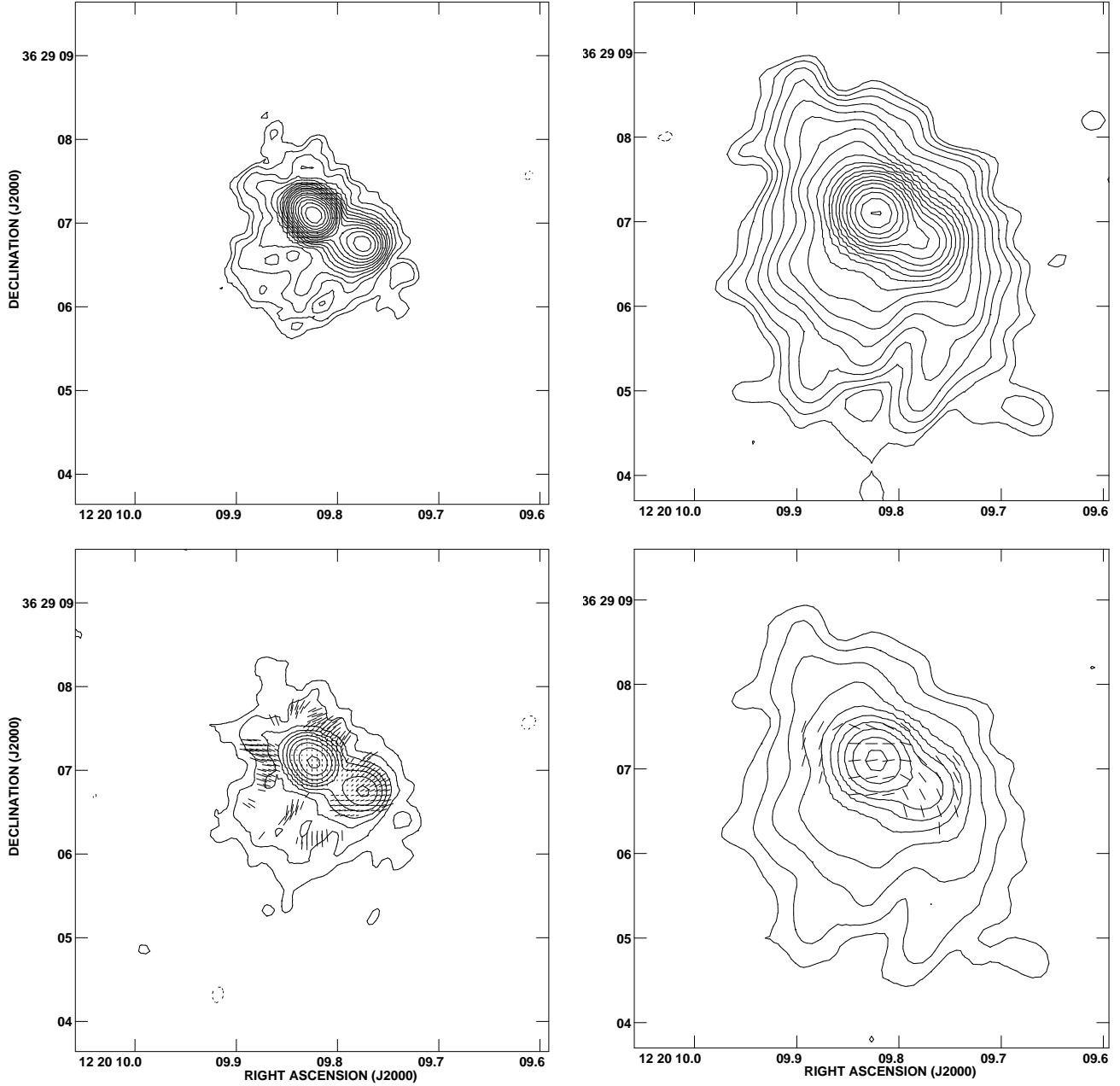


Figure 9: Maps of the radio source **1217+36**. (a – upper left) 8210 MHz total intensity map, FWHM 0.25 arcsec, with contours at  $85\mu\text{Jy beam}^{-1} \times (-1, 1, 1.414, 2, 2.828, 4 \dots 1024)$ . (b – upper right) 4710 MHz total intensity map, FWHM 0.45 arcsec, with contours at  $125\mu\text{Jy beam}^{-1} \times (-1, 1, 1.414, 2, 2.828, 4 \dots 1024)$ . (c – lower left) The 8210 MHz radio map with vectors of polarisation overlaid. A vector of length 0.36 arcsec corresponds to 100% polarisation. The contour levels are  $100\mu\text{Jy beam}^{-1} \times (-1, 1, 2, 4 \dots 1024)$ . (d – lower right) The magnetic field position angle, plotted wherever a rotation measure could be calculated.

redshift  $z = 1.00$  (Rawlings et al. 1998). The south-eastern core candidate is the brighter; the north-western has the flatter spectral index. With the current data it is impossible to unambiguously determine which is the core of the radio galaxy. We have aligned the infrared image by assuming, arbitrarily, that the north-western component is the core.

The second largest source in our sample, this radio source extends nearly 40 arcseconds. The south-eastern lobe

contains a double hotspot and shows very little polarised emission. The north-western lobe is more regular both in its structure and polarisation properties. Note that, as discussed at the beginning of this Section, the slightly speckled nature of the spectral index map close to the extremities of both lobes is likely to be an artefact caused by the inability of the CLEANING process to accurately represent smooth extended low-surface brightness emission.

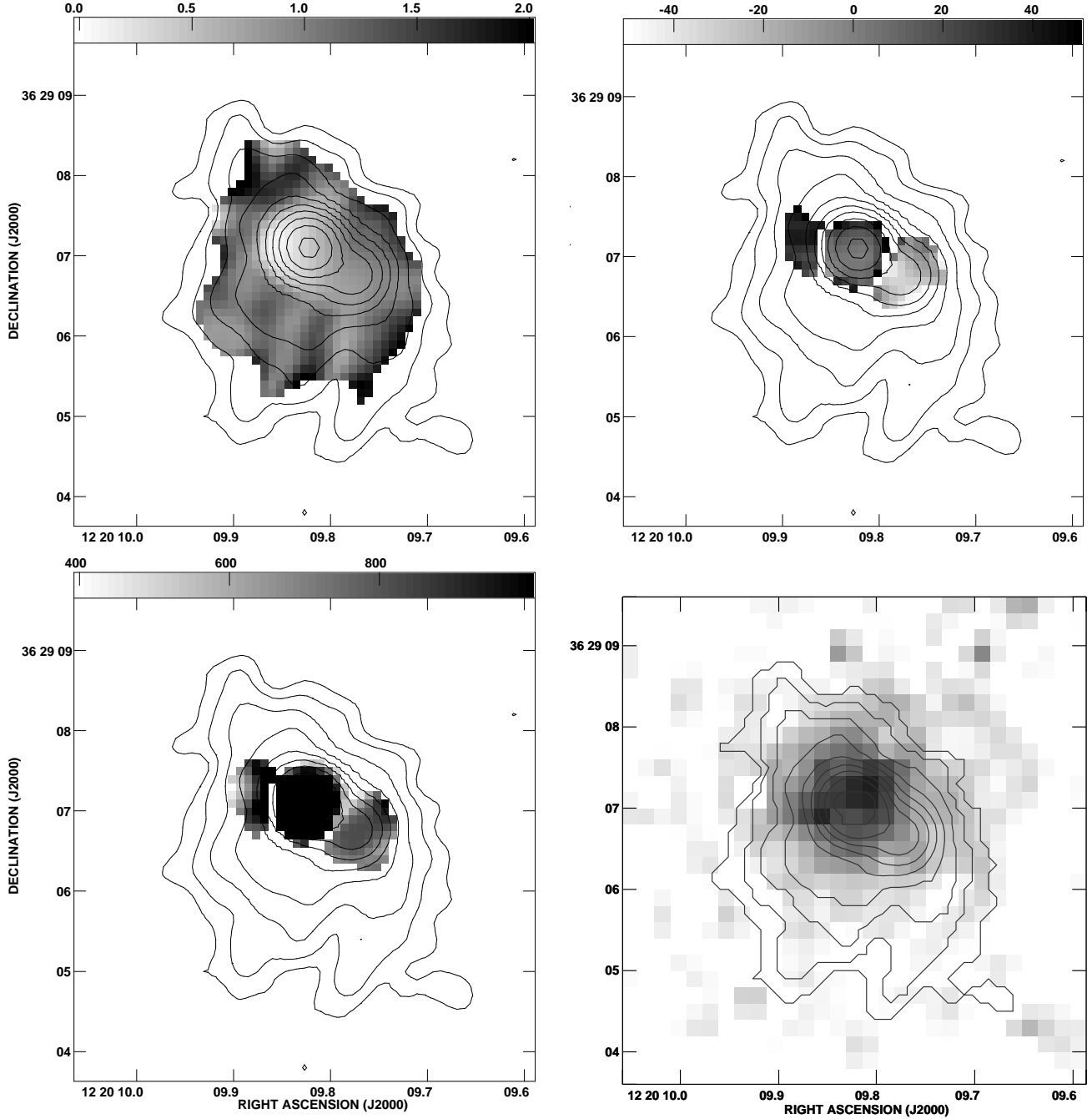


Figure 9: **cont.** (e – upper left) A spectral index map of the source, calculated between the frequencies 4710 and 8210 MHz. (f – upper right) A rotation measure map of the source, calculated from the frequencies 4535, 4885 and 8210 MHz. (g – lower left) A map of the depolarisation measure between 8210 and 4710 MHz (units in milli-ratios). (h – lower right) The 27-minute infrared K-band image taken using IRCAM3 on UKIRT. The contours of radio emission at 4710 MHz overlaid on figures (d) through to (h) are at  $150 \mu\text{Jy beam}^{-1} \times (-1, 1, 2, 4, \dots, 1024)$ .

#### 4 DISCUSSION

A number of features stand out in the radio data presented, and here we discuss these features and compare them with our sample of 3CR radio galaxies at redshift  $z \sim 1$  (Best et al. 1997), and with a sample of low redshift radio galaxies.

A comparison of the low-frequency radio power ( $P$ ) vs linear size ( $D$ ) diagram for the 6C radio galaxies and those in the 3CR sample within the overlapping redshift range  $0.85 \leq z \leq 1.5$  is shown in Figure 12, clearly demonstrating the lower radio power of the 6C radio galaxies. The aver-

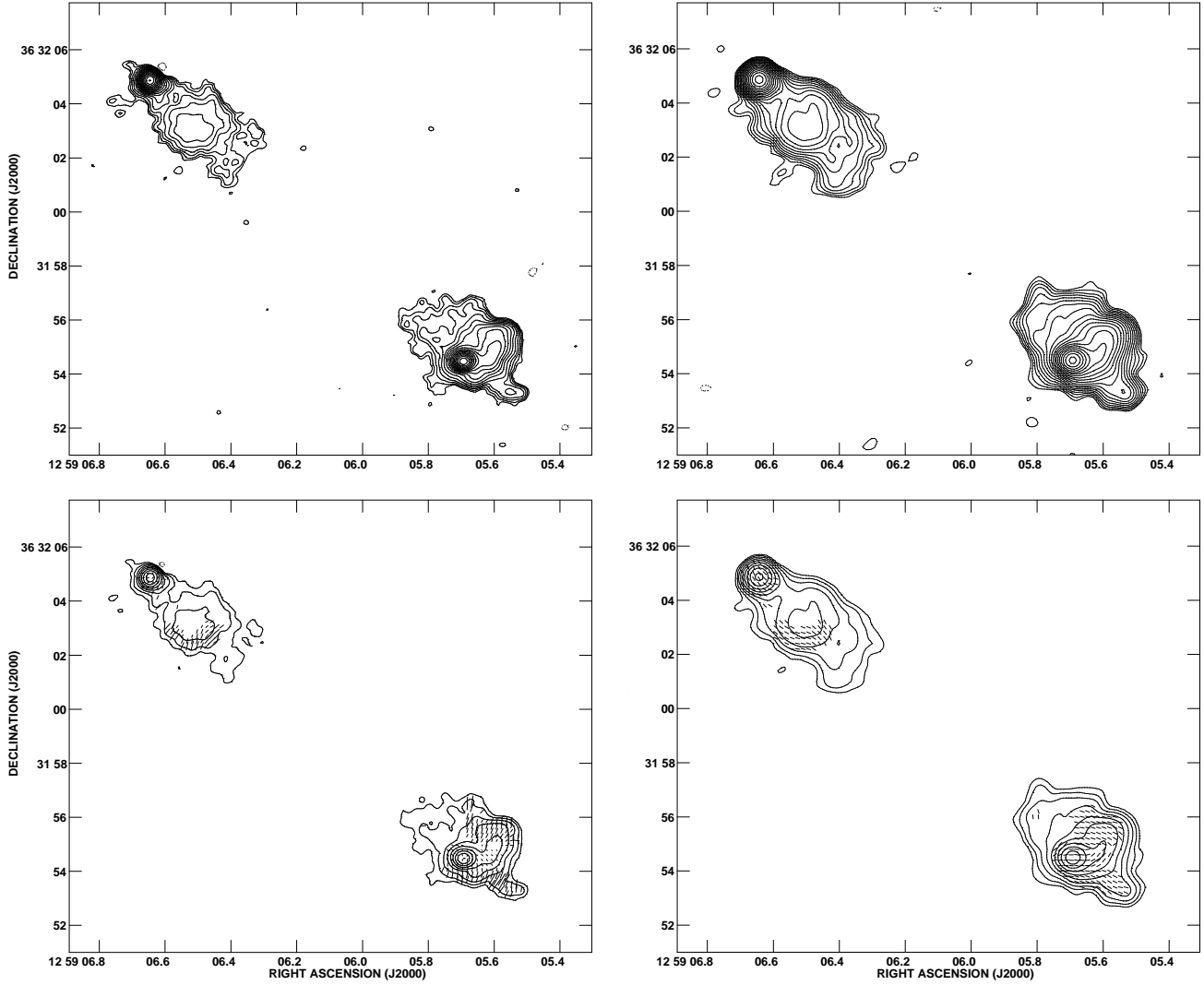


Figure 10: Maps of the radio source **1256+36**. (a – upper left) 8210 MHz total intensity map, FWHM 0.35 arcsec, with contours at  $60\mu\text{Jy beam}^{-1} \times (-1, 1, 1.414, 2, 2.828, 4 \dots 1024)$ . (b – upper right) 4710 MHz total intensity map, FWHM 0.55 arcsec, with contours at  $70\mu\text{Jy beam}^{-1} \times (-1, 1, 1.414, 2, 2.828, 4 \dots 1024)$ . (c – lower left) The 8210 MHz radio map with vectors of polarisation overlaid. A vector of length 0.72 arcsec corresponds to 100% polarisation. The contour levels are  $100\mu\text{Jy beam}^{-1} \times (-1, 1, 2, 4 \dots 1024)$ . (d – lower right) The magnetic field position angle, plotted wherever a rotation measure could be calculated.

age radio size of the 6C sources ( $D_{\text{mean}} = 137 \pm 35$  kpc;  $D_{\text{med}} = 102$  kpc, after re-including 1123+34 excluded from the sample by an angular size cut-off) is slightly smaller than that of the 3CR sources ( $D_{\text{mean}} = 222 \pm 49$  kpc;  $D_{\text{med}} = 155$  kpc): the difference falls part-way between the result of Oort et al. (1987), that the median linear size of radio sources increases with radio power according to  $D_{\text{med}} \propto P^m$  where  $m = 0.3 \pm 0.05$ , and that of Neeser et al. (1995) which showed no significant radio power dependence for radio sizes. The low number statistics in our small subsamples prohibits any significant conclusions from being drawn. The good overlap in linear sizes between the two samples does, however, mean that comparisons of the optical properties of these sources (Paper II) can safely be made.

#### 4.1 Radio core powers

In Table 2 we tabulate the core fraction,  $R$ , of the 6C subsample, defined as the ratio of the flux of the compact central component to that of the extended radio emission as measured at an observed frequency of 8 GHz; i.e.  $R = f_{\text{core}} / (f_{\text{total}} - f_{\text{core}})$ . With the exception of 1217+36 all of the cores appear unresolved. Due to the uncertainty in determining the core flux, 1217+36 is excluded from further analysis.

Core fractions were also determined for the sample of 3CR radio galaxies with redshifts  $z \sim 1$  of Best et al. (1997)<sup>\*</sup>, and a sample of 3CR FR II radio galaxies with

<sup>\*</sup> For some sources for which the data of Best et al. (1997) pro-



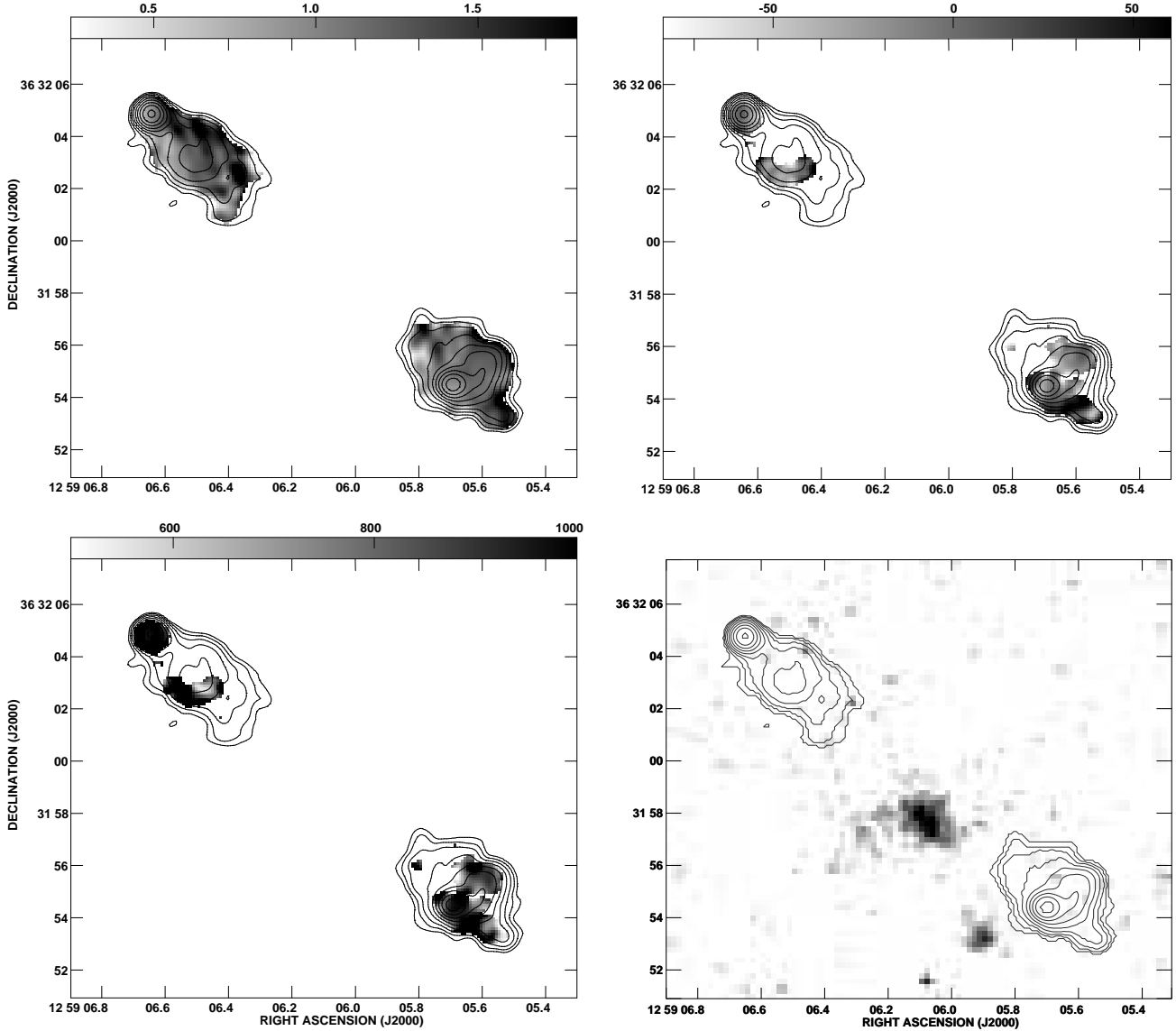


Figure 10: **cont.** (e – upper left) A spectral index map of the source, calculated between the frequencies 4710 and 8210 MHz. (f – upper right) A rotation measure map of the source, calculated from the frequencies 4535, 4885 and 8210 MHz. (g – lower left) A map of the depolarisation measure between 8210 and 4710 MHz (units in milli-ratios). (h – lower right) The 27-minute infrared K-band image, taken using IRCAM3 on UKIRT. The contours of radio emission at 4710 MHz overlaid on figures (d) through to (h) are at  $100\mu\text{Jy beam}^{-1} \times (-1, 1, 2, 4, \dots, 1024)$ .

redshifts  $z < 0.3$  described by Hardcastle et al. (1998). The eight objects classified as broad-line radio galaxies have been excluded from the latter sample, since the closer orientation of the radio axes of these objects to the line of sight

vided only upper limits to the core fractions, values are available from the literature: 3C324 and 3C368 (Best et al. 1998a); 3C49 and 3C241, by interpolating the core flux densities at 5 and 15 GHz (Fanti et al. 1989; Akujor et al. 1991; van Breugel et al. 1992) to 8 GHz; 3C337 (Pedelty et al. 1989b) has a 5 GHz core flux available, from which an 8 GHz flux can be derived to within a factor of two, assuming the core spectral index to lie between  $-0.5$  and  $1$  — in the figures, this point is plotted at the centre of this range, together with an error bar.

than that of narrow-line radio galaxies leads to Doppler boosting of the central cores, enhancing their  $R$  value (e.g. Morganti et al. 1997, Hardcastle et al. 1998). For the same reason, 3C22 was excluded from the high redshift 3CR sample (Rawlings et al. 1995; Economou et al. 1995). Further, to allow a comparison between the low and high redshift samples, account must be taken of the difference in rest-frame frequency due to the different spectral indices of the core and extended emission regions. For this reason, the core fractions of the low redshift sources have been adjusted to the values that would be measured at rest-frame 16 GHz (observed frame 8 GHz for a source at redshift  $z = 1$ ) under the assumption that the cores have a flat radio spectrum and the lobes have  $\bar{\alpha} \sim 0.8$ .

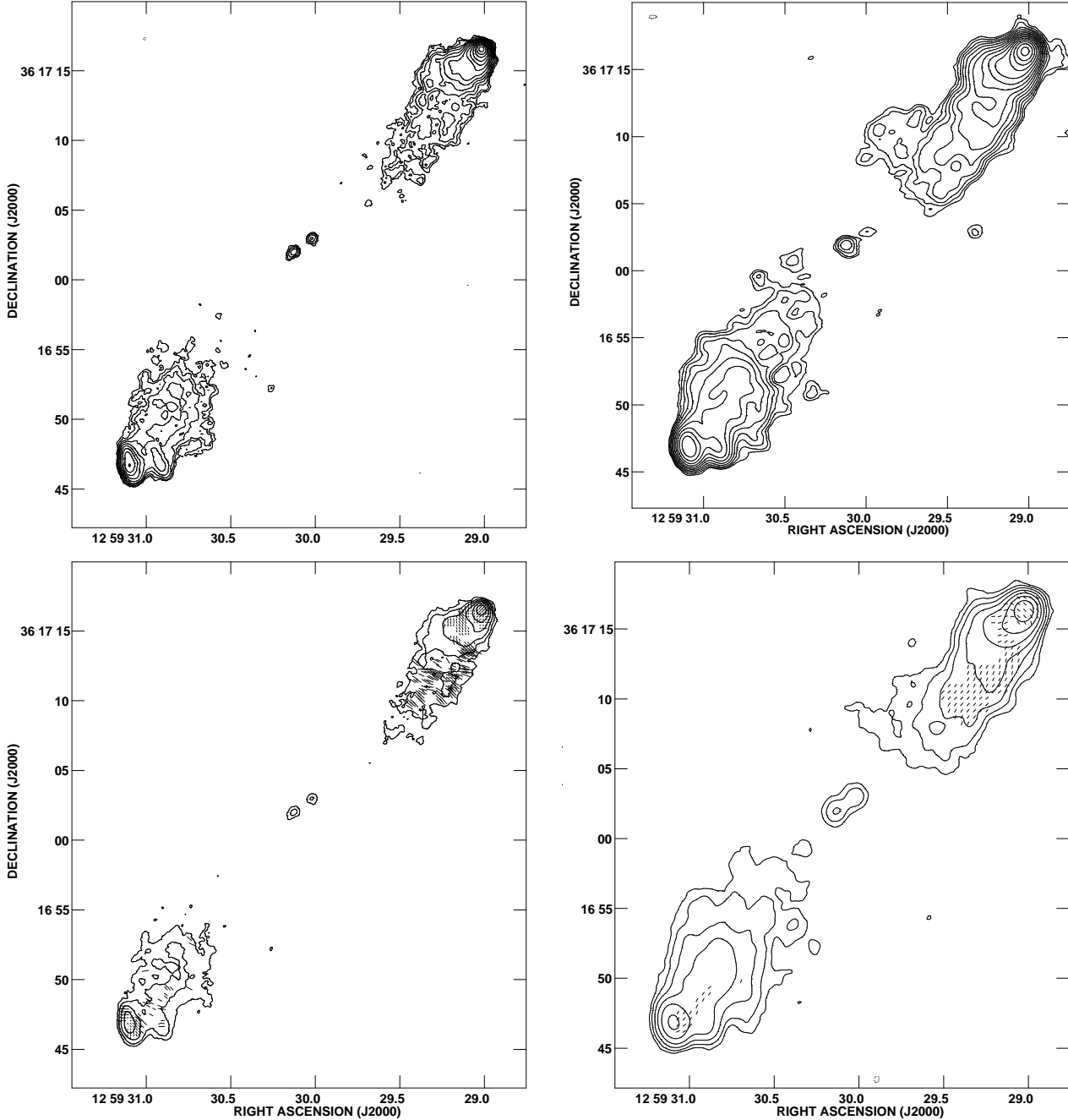


Figure 11: Maps of the radio source **1257+36**. (a – upper left) 8210 MHz total intensity map, FWHM 0.6 arcsec, with contours at  $45\mu\text{Jy beam}^{-1} \times (-1, 1, 1.414, 2, 2.828, 4 \dots 1024)$ . (b – upper right) 4710 MHz total intensity map, FWHM 1.0 arcsec, with contours at  $80\mu\text{Jy beam}^{-1} \times (-1, 1, 1.414, 2, 2.828, 4 \dots 1024)$ . (c – lower left) The 8210 MHz radio map with vectors of polarisation overlaid. A vector of length 0.84 arcsec corresponds to 100% polarisation. The contour levels are  $60\mu\text{Jy beam}^{-1} \times (-1, 1, 2, 4 \dots 1024)$ . (d – lower right) The magnetic field position angle, plotted wherever a rotation measure could be calculated.

In general, the core fraction of a radio source depends most strongly upon its orientation, through Doppler boosting effects. Here, however, since we have begun by selecting samples from low frequency radio surveys, and then excluded the quasar and broad-line radio galaxy populations,

it has been possible to restrict our analysis to sources oriented close to the plane of the sky where beaming effects are of little importance. The measured core fractions therefore reflect an intrinsic property of the radio sources.

In Figure 13, the core fraction is plotted against the

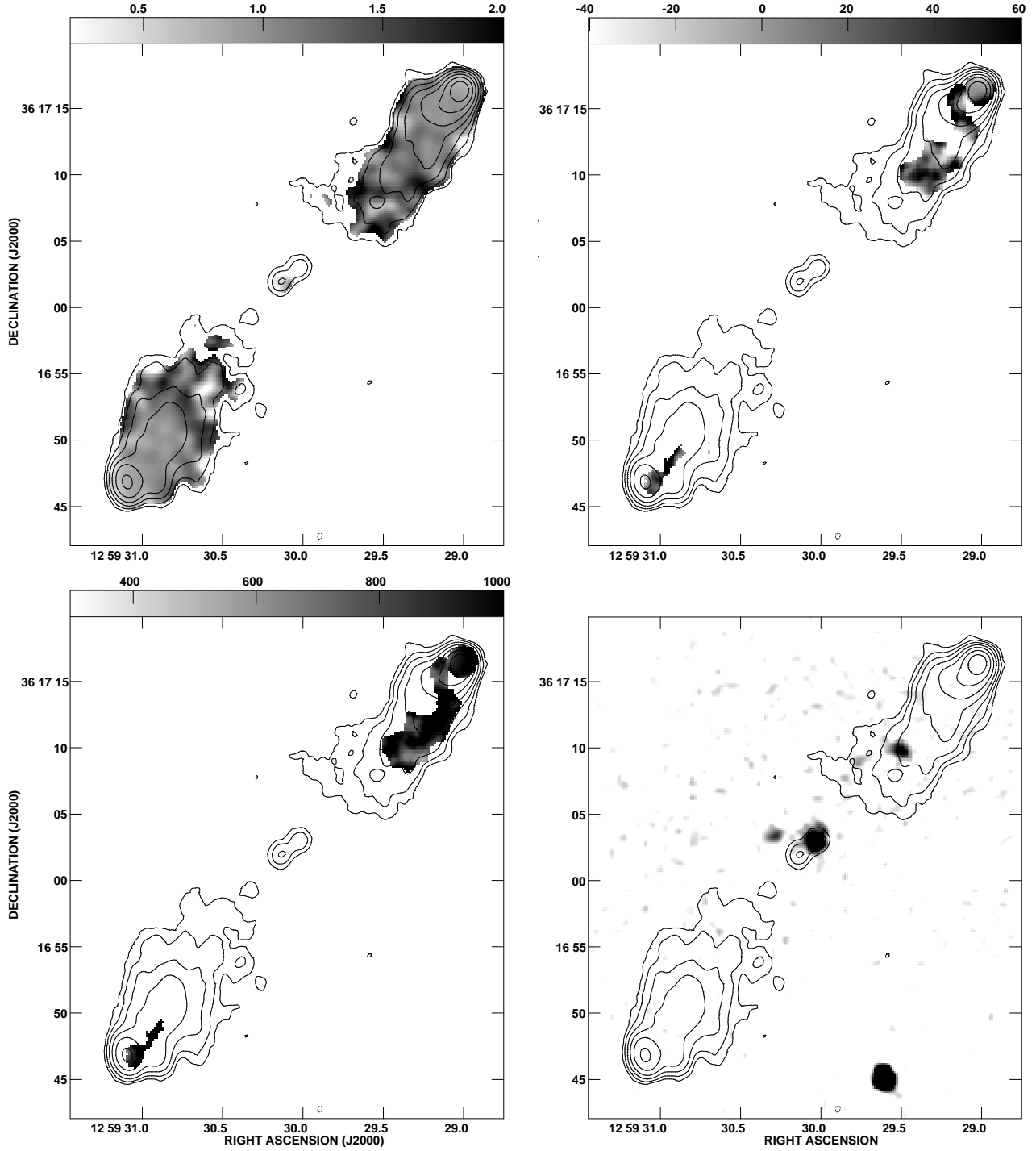
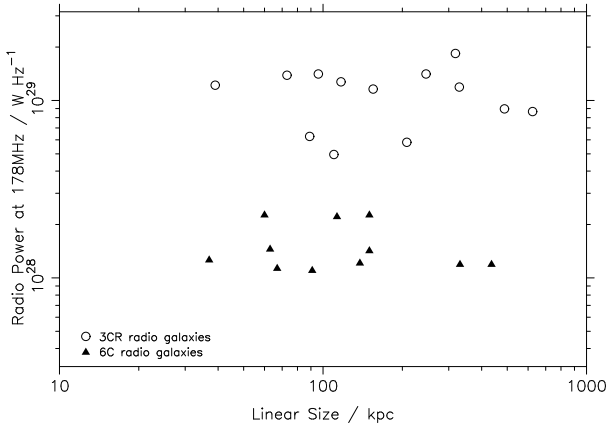
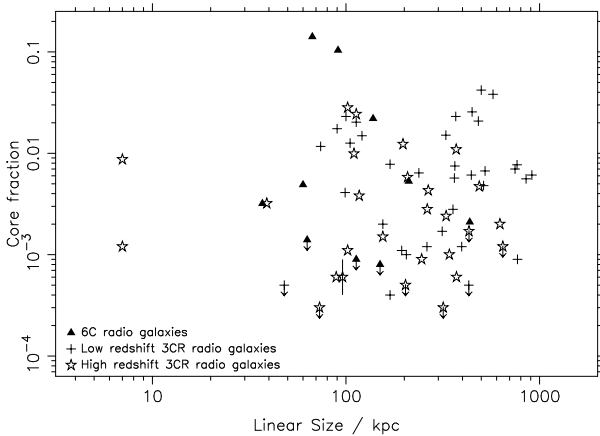


Figure 11: **cont.** (e – upper left) A spectral index map of the source, calculated between the frequencies 4710 and 8210 MHz. (f – upper right) A rotation measure map of the source, calculated from the frequencies 4535, 4885 and 8210 MHz. (g – lower left) A map of the depolarisation measure between 8210 and 4710 MHz (units in milli-ratios). (h – lower right) The 22-minute infrared K-band image taken using the REDEYE camera on the CFHT. The radio maps at 8210 MHz overlaid on figures (d) through to (h) have FWHM 1.25 arcsec and contour levels at  $50 \mu\text{Jy beam}^{-1} \times (-1, 1, 2, 4 \dots 1024)$ .



**Figure 12.** The radio power ( $P$ ) versus linear size ( $D$ ) diagram from the 6C radio galaxies presented here and the 3CR radio galaxies from the sample of Best et al. (1997) in the overlapping redshift range.



**Figure 13.** A plot of core fraction at a rest-frame of approximately 16 GHz versus linear radio size for the 6C radio galaxies presented here, the  $z \sim 1$  3CR radio galaxies from the sample of Best et al. (1997), and a low redshift ( $z < 0.3$ ) sample of 3CR galaxies from the sample of Hardcastle et al. (1998). See text for more details.

linear size of the radio source for each of the three samples; no significant correlation is seen. This lack of correlation naively implies a strong self-similarity in the growth of FR II radio sources. Models of the evolution of FR II radio sources through the P–D diagram (e.g. Kaiser et al. 1997 and references therein) indicate, however, that as the size of a radio source increases from about 10 kpc to a few hundred kpc, the radio luminosity of its lobes will fall by about a factor of 3. The core flux is not expected to change during this period, thus resulting in a theoretical increase in the core fraction with linear size. Figure 13 shows only little evidence for such an increase; the median core fraction for the sources smaller than 100 kpc is 0.0037, increasing to 0.0056 for the sources larger than 300 kpc. At any given linear size there is a large scatter in the core fractions, and so to properly investigate this result it is important to sample a wider range of linear sizes than is possible here, by adding to the current diagram a well-defined sample of compact sources and, more importantly, a sample of giant radio galaxies ( $D \gtrsim 1$  Mpc)

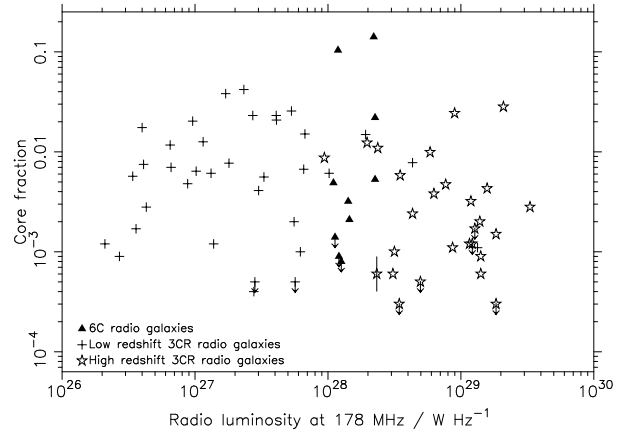


**Figure 14.** A plot of 8 GHz core fraction versus radio luminosity for the same samples as Figure 13.

where the fall-off of lobe flux with radio size is expected to be strong.

Figure 14 shows the same core fraction parameter plotted against the total radio luminosity of the source. There is only a very weak (92% significant in a Spearman Rank test) inverse correlation between these parameters, over three orders of magnitude in radio luminosity. Equivalently, for the combined samples we derive a tight correlation between the core flux and the extended flux, with a best-fitting power-law function of  $P_{\text{core}} \propto P_{\text{extended}}^{0.74 \pm 0.06}$  (see also e.g. Fabbiano et al. 1984, who found  $P_{\text{core}} \propto P_{\text{total}}^{0.75 \pm 0.05}$  within a sample of low redshift 3CR FRI and FRII sources).

This latter result is particularly interesting when viewed with reference to the question of why powerful radio sources are so powerful. The nearby radio galaxy Cygnus A, for example, is approximately 1.5 orders of magnitude more radio luminous than any other nearby FRII radio galaxy, but Barthel and Arnaud (1996) have pointed out that its far-infrared luminosity, AGN X-ray luminosity and integrated emission line luminosity are not extreme. They therefore suggest that the ‘anomalous’ radio loudness of Cygnus A, and other powerful radio sources, are entirely attributable to their location in a cluster: the denser surrounding medium reduces the expansion losses of the synchrotron electron population, resulting in a more efficient transfer of AGN power into radio emission.

Whilst this effect is undoubtedly important, if this were the only responsible process then the radio core emission of Cygnus A and other powerful radio galaxies should not be enhanced, and their core fractions should consequently be low. In fact, Cygnus A (one of our low redshift 3CR sample) can be seen on Figure 14 at  $P = 1.3 \times 10^{29}$ ,  $R = 0.0011$ ), in a similar location to the powerful high redshift 3CR sources. Its core fraction is within the range of values of the other sources in the low redshift sample, although at the lower end of that; its core flux density is the highest within that sample. This result means that the high radio power of Cygnus A must arise primarily due to a high radio power of its AGN. The dense surrounding environment may further boost its radio power, resulting in its lower than average core fraction, but this can not be the dominant effect.

Generalising this result to the whole sample, the implication of the strong radio core power versus extended power

correlation is that the high radio powers of the most powerful sources must originate in the AGN. The fact that the coefficient of the correlation power-law is less than unity ( $P_{\text{core}} \propto P_{\text{extended}}^{0.74 \pm 0.06}$ ), however, leaves scope for, and indeed requires, an additional effect which is likely to be environmental.

#### 4.2 Core spectral indices

A second interesting feature of the radio cores is their spectral index properties. At low redshifts, radio source cores generally have flat or inverted spectra  $-1 < \alpha < 0.5$ , whilst recent results have shown that the radio cores in samples of radio galaxies with redshifts  $z \gtrsim 2$  often have steep spectra,  $\alpha > 0.5$ , between observed frequencies of 5 and 8 GHz (Carilli et al. 1997; Athreya et al. 1997). Lonsdale et al. (1993) and Athreya et al. (1997) have interpreted this as being due not to a cosmic epoch effect, but simply to the different rest-frame frequencies at which the high and low redshift samples are observed. In their models, the cores of all radio sources are flat due to synchrotron self absorption at low frequencies, but steepen rapidly above about 20 GHz, the precise break frequency varying slightly from source to source.

The 6C sources show a wide range in core spectral indices: in five cases the spectral index is flat or inverted; the ‘core’ of 1217+36 has an intermediate spectral index, but contamination from lobe emission suggests that the true core will be flatter; 1257+36 may have a flat or steep spectrum core, depending upon which candidate is the true core; 1204+35 is a clear case of a steep spectrum core. Interestingly, this last source is also one of the highest redshift objects in the sample ( $z = 1.37$ ), and would fit the picture described above if it was an example of a source with a low average break frequency.

There is, unfortunately, no large sample of 3CR radio galaxies at this redshift for which sufficiently deep two-frequency radio observations have been made to obtain core spectral indices. The few cases for which these measurements are available have also provided varied results, for example from the inverted core ( $\alpha \approx -0.17$ ) of 3C49 (van Breugel et al. 1992; Fanti et al. 1989) to a relatively steep spectrum core ( $\alpha = 0.54$ ) in 3C368 (Best et al. 1998a).

#### 4.3 Rotation measure properties

The mean rotation measures determined for the 6C radio galaxies are in no cases extreme, generally being below  $40 \text{ rad m}^{-2}$ . In many sources, however, there is a significant difference between the mean values determined for the two lobes, and in some instances strong gradients are seen within individual lobes in the depolarisation and rotation measure maps. Such large variations are unlikely to have their origin in our galaxy (Leahy 1987), instead being caused by gas in the neighbourhood of the radio sources, meaning that the rest-frame rotation measures are a factor of  $(1+z)^2$  larger than those quoted in Table 3.

The large rotation measure differences between the radio lobes of the 6C sample,  $102 \text{ rad m}^{-2}$  in the rest-frame on average, are in stark contrast to the study by Simonetti and Cordes (1986) who found typically less than  $10 \text{ rad m}^{-2}$

difference between the two lobes of low redshift 3C and 4C radio sources. Steep gradients in the depolarisation and rotation measure are indicative of a dense and clumpy environment surrounding the radio source, suggesting that the 6C sources with redshifts  $z \sim 1$  lie in a denser environment than those nearby. An interesting question is whether this increase of environmental density correlates with radio power or with redshift; Cygnus A, a low redshift source of comparable radio power to the distant 3CR sources, shows an extreme range of rotation measures ( $-4000$  to  $+3000 \text{ rad m}^{-2}$ ; Dreher et al. 1987) supporting the former.

Pedelty et al. (1989a) determined the rotation measures of a sample of 12 high redshift 3CR radio galaxies at somewhat lower angular resolution (typical beam-size  $\sim 1.5''$ ), and found a mean rest-frame difference of about  $175 \text{ rad m}^{-2}$  between the two radio lobes, a value even more extreme than that of the current 6C sample. They also observed structure within the lobes, particularly in the case of 3C337 (Pedelty et al. 1989b). Johnson et al. (1995) selected three high redshift 3CR radio sources with angular scales in excess of 40 arcsecs, and also found considerable rotation measure structure within individual lobes. Best et al. (1998a) studied two radio galaxies from the Pedelty et al. sample, 3C324 and 3C368, with the same high angular resolution obtained for the observations presented in this paper, and found considerable structure on scales smaller than those previously probed. Gradients of up to  $1000 \text{ rad m}^{-2}$  over distances of about 10 kpc were measured. If the results from these small samples are representative of the  $z \sim 1$  3CR sources, then it would suggest that the distant 3CR sources live in still denser environments than the 6C sources at the same redshift.

#### 4.4 Separation Quotients

The separation quotient,  $Q$ , is defined as the ratio  $Q = \theta_1/\theta_2$ , where  $\theta_1$  and  $\theta_2$  are the angular distances from the nucleus of the more distant and closer hot-spots respectively (Ryle & Longair 1967; Longair & Riley 1979). These arm-lengths are tabulated in Table 3, and the separation quotients in Table 2. The 6C galaxies show considerable asymmetries, with a mean value of  $\bar{Q} = 1.80 \pm 0.28$ , although this is somewhat dominated by the very high asymmetries of 0943+39 and 1017+37; the median value of  $Q$  for the sample is 1.47. This can be compared to 3CR radio galaxies in the same redshift range which have  $\bar{Q} = 1.39 \pm 0.07$ , with a median value of 1.37 (data taken from Best et al. 1995, 1997). The 6C galaxies appear to show higher asymmetry quotients, although to obtain statistically significant confirmation study of a larger sample of lower power sources at these redshifts, such as those in the Molonglo Strip (McCarthy et al. 1997) will be required.

The separation quotient has two origins. Firstly, the light-travel time differences from the two hotspots for any source which is not orientated precisely in the plane of the sky will give rise to an apparent asymmetry: this has been used by a number of authors to investigate hotspot advance speeds (Longair & Riley 1979; Banhatti 1980; Best et al. 1995; Scheuer 1995). Secondly, environmental effects may produce intrinsic asymmetries (e.g. McCarthy et al. 1991). Best et al (1995) compared radio galaxies and quasars using this method to test orientation-based unification schemes

(Barthel 1989), and suggested that for radio galaxies the two effects are roughly comparable. In this respect, a higher separation quotient for the 6C sources at these redshifts would be an interesting result, possibly reflecting a greater environmental influence on the lower power jets of the 6C sources.

## 5 CONCLUSIONS

We have presented total intensity, spectral index, polarisation and rotation measure radio maps of a complete sample of eleven galaxies from the 6C catalogue, together with infrared images of the fields surrounding them. Basic source parameters were also tabulated. The data were compared with a sample of more powerful 3CR radio galaxies at the same redshift, and with a low redshift radio galaxy sample. The main results can be summarized as follows.

- All of the sources display an FR II type morphology, with the possible exception of 1217+36 in which the compact central double component is surrounded by an extended halo of radio emission. Most of the sources, however, show some deviation from the ‘standard double’ morphology, either as double hotspots or hotspots lying withdrawn from the leading edge of the lobe.

- We have detected radio cores in eight of the eleven sources, four for the first time, co-incident with the optical identifications. In at least two, and possibly as many as five cases, the core is inverted. In one case the core has a steep spectrum ( $\alpha \sim 0.9$ ), consistent with the trend for radio cores at high redshifts to high steeper spectral indices (Carilli et al. 1997; Athreya et al. 1997).

- The ratio of radio luminosity of the core to that of the extended emission,  $R$ , appears to increase less rapidly with the linear size of the radio source than predicted by radio source evolution models. It is only weakly anti-correlated with the total radio power, implying that the total radio power of a radio source is determined primarily by the AGN. Environmental effects play a secondary role.

- The rotation measures detected are in no cases extreme (generally averaging below  $40 \text{ rad m}^{-2}$ ), but strong gradients are seen in both the depolarisation and rotation measures between the two lobes and often within individual lobes. These gradients are significantly larger than those of low redshift radio sources, suggesting that the 6C sources live in a dense, clumpy environment. On the other hand, they appear lower than those of the 3CR sources at the same redshift, possibly indicating a weak dependence of radio power on local environmental density.

## ACKNOWLEDGEMENTS

The National Radio Astronomy Observatory is operated by Associated Universities Inc., under co-operative agreement with the National Science Foundation. This work was supported in part by the Formation and Evolution of Galaxies network set up by the European Commission under contract ERB FMRX-CT96-086 of its TMR programme. We thank the referee, Dr T.W.B. Muxlow, for useful comments.

## REFERENCES

- Akujor C. E., Spencer R. E., Zhang F. J., Davis R. J., Browne I. W. A., Fanti C., 1991, *MNRAS*, 250, 215
- Allington-Smith J. R., Lilly S. J., Longair M. S., 1985, *MNRAS*, 213, 243
- Allington-Smith J. R., Perryman M. A. C., Longair M. S., Gunn J. E., Westphal J. A., 1982, *MNRAS*, 201, 331
- Athreya R. M., Kapahi V. K., McCarthy P. J., van Breugel W. J. M., 1997, *MNRAS*, 289, 525
- Banhatti D. G., 1980, *A&A*, 84, 112
- Barthel P. D., 1989, *ApJ*, 336, 606
- Barthel P. D., Arnaud K. A., 1996, *MNRAS*, 283, L45
- Benítez N., Martínez-González E., Gonzalez-Serrano J. I., Cayon L., 1995, *AJ*, 109, 935
- Best P. N., Bailer D. M., Longair M. S., Riley J. M., 1995, *MNRAS*, 275, 1171
- Best P. N., Carilli C. L., Garrington S. T., Longair M. S., Röttgering H. J. A., 1998a, *MNRAS*, 299, 357
- Best P. N., Longair M. S., Röttgering H. J. A., 1996, *MNRAS*, 280, L9
- Best P. N., Longair M. S., Röttgering H. J. A., 1997, *MNRAS*, 292, 758
- Best P. N., Longair M. S., Röttgering H. J. A., 1998b, *MNRAS*, 295, 549
- Carilli C. L., Röttgering H. J. A., van Ojik R., Miley G. K., van Breugel W. J. M., 1997, *ApJ Supp.*, 109, 1
- Chambers K. C., Miley G. K., van Breugel W. J. M., 1987, *Nat.*, 329, 604
- Dreher J. W., Carilli C. L., Perley R. A., 1987, *ApJ*, 316, 611
- Eales S. A., 1985, *MNRAS*, 217, 149
- Eales S. A., Rawlings S., Law-Green D., Cotter G., Lacy M., 1997, *MNRAS*, 291, 593
- Economou F., Lawrence A., Ward M. J., Blanco P. R., 1995, *MNRAS*, 272, L5
- Fabbiano G., Trinchieri G., Elvis M., Miller L., Longair M., 1984, *ApJ*, 277, 115
- Fanti C., Fanti R., Parma P., Venturi T., Schilizzi R. T., Nan Rendong Spencer R. E., Muxlow T. W. B., van Breugel W. J. M., 1989, *A&A*, 217, 44
- Hardcastle M. J., Alexander P., Pooley G. G., Riley J. M., 1998, *MNRAS*, 296, 445
- Johnson R. A., Leahy J. P., Garrington S. T., 1995, *MNRAS*, 273, 877
- Kaiser C. R., Dennett-Thorpe J., Alexander P., 1997, *MNRAS*, 292, 723
- Laing R. A., Riley J. M., Longair M. S., 1983, *MNRAS*, 204, 151
- Law-Green J. D. B., Leahy J. P., Alexander P., Allington-Smith J. R., van Breugel W. J. M., Eales S. A., Rawlings S. G., Spinrad H., 1995, *MNRAS*, 274, 939
- Leahy J. P., 1987, *MNRAS*, 226, 433
- Lilly S. J., 1989, *ApJ*, 340, 77
- Lilly S. J., Longair M. S., 1984, *MNRAS*, 211, 833
- Longair M. S., Best P. N., Röttgering H. J. A., 1995, *MNRAS*, 275, L47
- Longair M. S., Riley J. M., 1979, *MNRAS*, 188, 625
- Lonsdale C. J., Barthel P. D., Miley G. K., 1993, *ApJ Supp.*, 87, 63
- McCarthy P. J., 1993, *ARA&A*, 31, 639
- McCarthy P. J., Kapahi V. K., van Breugel W. J. M., Persson S. E., Athreya R., Subramhanya C. R., 1997, *ApJ Supp.*, 107, 19
- McCarthy P. J., van Breugel W. J. M., Kapahi V. K., 1991, *ApJ*, 371, 478
- McCarthy P. J., van Breugel W. J. M., Spinrad H., Djorgovski S., 1987, *ApJ*, 321, L29
- Morganti R., Oosterloo T. A., Reynolds J. E., Tadhunter C. N., Migenes V., 1997, *MNRAS*, 284, 541

- Naundorf C. E., Alexander P., Riley J. M., Eales S. A., 1992, MNRAS, 258, 647
- Neeser M. J., Eales S. A., Law-Green J. D., Leahy J. P., Rawlings S., 1995, ApJ, 451, 76
- Oort M. J. A., Katgert P., Windhorst R. A., 1987, Nat, 328, 500
- Pedelty J. A., Rudnick L., McCarthy P. J., Spinrad H., 1989a, AJ, 97, 647
- Pedelty J. A., Rudnick L., McCarthy P. J., Spinrad H., 1989b, AJ, 98, 1232
- Rawlings S., Eales S. A., Lacy M., 1998, in preparation
- Rawlings S., Lacy M., Sivia D. S., Eales S. A., 1995, MNRAS, 274, 428
- Ryle M., Longair M. S., 1967, MNRAS, 136, 123
- Scheuer P. A. G., 1995, MNRAS, 277, 331
- Simonetti J. H., Cordes J. M., 1986, ApJ, 310, 160
- Thompson D., Djorgovski S., Vigotti M., Grueff G., 1994, AJ, 108, 828
- van Breugel W. J. M., Fanti C., Fanti R., Stanghellini C., Schilizzi R. T., Spencer R. E., 1992, A&A, 256, 56